 doi:10.20944/preprints202205.0204.v1

Article

Power Quality Enhancement For Decentralized Microgrids in Island Mode

Muhammad Arshad Rasheed [1,2], Hasan Erteza Gelani [2,*], Hira Tahir[2], Muhammad Irfan Abid[1] and Faisal Saeed[3,*]

[1] Department of Electrical Engineering & Technology, Faisalabad Campus, Riphah International University, Punjab 38000, Pakistan
[2] Department of Electrical Engineering, University of Engineering and Technology Lahore, Faisalabad Campus, Faisalabad, 38000, Punjab, Pakistan
[3] SBA School of Science and Engineering, Lahore University of Management Sciences, Lahore, Punjab, 54792, Pakistan
* Correspondence: Hasan Erteza Gelani- erteza.gelani@uet.edu.pk ; Faisal Saeed -19060005@lums.edu.pk

Abstract: The microgrid is a small-scale, autonomous decentralized power plant with its own distributed generation, storage capacity and multiple loads, with the capacity to function in grid interconnected and an island mode. The decentralized control of microgrids with parallel operated voltage source converters (VSCs) is proposed in this paper to improve power quality using a machine learning approach. The DNN based MPPT controller is proposed and its best performance is presented. The SRF-PLL is utilized for AC side synchronization in VSC control. The proposed microgrid involves two PV arrays fed to two voltage source converters along with their independent controls, connected in parallel through LC filters and line coupling transformers and serves the loads at PCC. The proposed model is simulated using MATLAB/Simulink. The dq-framed inner loop control is employed to individually regulate the real and reactive power at the point of common coupling. Furthermore, the proposed model is analyzed and compared by employing a mathematical model of AC system dynamics, inner loop control, output voltage quality, AC harmonic spectrum analysis, and total harmonic distortion (THD) in both grid interconnected and island mode. In island mode, AC harmonic spectrum and THD are accomplished within the permissible range.

Keywords: microgrid; DNN; parallel inverters; island mode; power quality

1. Introduction

A microgrid is a small decentralized power plant with its own generation and storage capacity as well as definable boundaries. The microgrid is the most effective and reliable solution of integration of DGs with witch capacity to function in grid interconnected and an island mode [1].

Island microgrid systems typically exist at remote locations (e.g. remote villages or remote industrial areas) where the main grid interconnection is not possible because of technological or economic restrictions. The objective is to reduce diesel fuel by incorporating photovoltaic (PV), distributed wind and/or river hydroelectricity [2].

The island microgrid control is complicated because the frequency and voltage control of the controller must be reinforced, and the power control between DG units must be sufficient [3]. The key actuators in AC microgrid are voltage source converters and due to power capacity limitations, converters operate in parallel to improve system reliability with critical loads [4].

The parallel-connected converters control is the confrontation to achieving high-quality load or power-sharing with voltage magnitude constancy, less frequency oscillations and total harmonics distortion (THD) within the permissible range [5].

Preprints (www.preprints.org) | NOT PEER-REVIEWED | Posted: 16 May 2022 doi:10.20944/preprints202205.0204.v1

2. Literature Survey

The rising urge for low-cost, high-quality power converters for parallel-connected voltage source converters in island mode has motivated the researchers to make impactful and gainful research in the related field. The parallel-connected converter control topologies are based on wired [6] or wireless controllers [7]. Wired control ensures reliability and effective power-sharing based on contact links between converter modules whereas wireless control is more stable, however, presents the reduction in reliability of service [8].

Control techniques based on master-slave communication (wired control) may be successful in achieving high power quality power-sharing [9]. This is unfeasible in remote areas because of techno-economic obstacles such as device expenditure and expansiveness. As a result, it is preferable to share power without requiring an external connection (wireless control) [9, 10]. Table 1 and Table 2 summarize various control strategies employed for controlling parallel inverters.

Table 1. Wireless control strategies for parallel inverters [9, 10].

Control Strategies for Parallel Inverters		
Wireless Control		
1. Conventional droop controller	i.	Frequency and voltage droop control
	ii.	Phase angle droop control
	iii.	Voltage based droop control
2. Droop control with varying output impedance	i.	Global droop controller
	ii.	Essential impedance base droop controller
	iii.	Conventional impedance method
	iv.	Enhance virtual method
	v.	Adaptive virtual impedance method
3. Signal injection method-based droop controller	i.	Harmonic virtual impedance method
	ii.	Hybrid droop controller.
4. Droop control improve transient responses.		

Table 2. Wired control strategies for parallel inverters [9, 10].

Communication based or Wired Control		
1. Common Duty Ratio Control		
2. Centralized Control	i.	CMC-Central Mode Control
	ii.	CLC-Central Limit Control
3. Active Current Distribution Control	i.	IACS Control
	ii.	Master Slave Control
	iii.	Circular Chain Control

In common duty ratio control [6], without monitoring system output voltages or currents, the duty ratio from the current controller is rendered common to all remaining inverter modules working in parallel, and therefore the current is shared evenly. Central mode control [11] is made up of a voltage and current controller with independent control loops for controlling output voltage and load current. Central Limit Control [12] referred the output currents of each converter follow the reference limited current. The IACS is conventional load current-based control[13] technology where the inverter module output current is routed to a current sharing bus, which produces a suitable reference current signal that equalizes each inverter's maximum value.

In master-slave control [14], the voltage control output of the master inverter acts as the reference current signal for the slave inverters. Since wireless control schemes skip

Preprints (www.preprints.org) | NOT PEER-REVIEWED | Posted: 16 May 2022 doi:10.20944/preprints202205.0204.v1

vital communicational lines between inverter units, they have an advantage over current-sharing control strategies. As a result, the droop approach is more dependable, scalable, and modular in design.

The droop method is based on the concept of integrating real and reactive power with voltage and frequency. In voltage and frequency drop control, active power is determined by power angle and reactive power is regulated by output voltage magnitude. This is referred as the P/Q droop method [7]. While the traditional droop controller is efficient, it has a number of flaws, including the failure to meet various control goals, the resistive design of low-voltage dissemination lines [15], non-linear loads ineffectiveness and inaccuracy of reactive power regulation [16].

An energy storage-free control scheme proposed in [17], which employed the pulse width modulation for power monitoring from PV modules and speed control of fuzzy logic-based diesel generators. A distributed secondary control was investigated in [18], to maintain the rated voltage in a stand-alone micro-grid. Multiple machine learning models are used to offer secondary control when a primary control scheme is insufficient to maintain a steady voltage following a rapid shift in load.

A neuro-dynamic programming approach based on fuzzy critique is employed in [19] for online tuning of PI coefficients to assess and regulate the active and reactive powers of voltage source converter in microgrids. In [20], the frequency and voltage oscillations in an island microgrid are minimized, and optimum droop controller parameters are determined using a frog algorithm that considers line efficacy.

Another well-known technology for intelligent tuning is the NN (Neural-network), utilized by the authors of [21], to enhance the current relative integral regulation and regulate the output frequency and voltages of an autonomous micro grid. The parameters in the majority of articles that employed online-tuning techniques for the PI coefficient of microgrids are chosen without adequate resiliency against diverse disruptions based on a hit and trial basis.

In this paper, decentralized control of microgrid having parallel-connected VSCs is proposed, to enhance power quality by using the machine learning approach. The DNN based MPPT controller is proposed and its best performance is presented. The SRF-PLL is utilized for AC side synchronization in VSCs control.

The proposed microgrid involves two PV arrays fed to two voltage source converters along with their independent controls, connected in parallel through LC filters and line coupling transformers. The loads are served at the point of common coupling PCC, the complete model is pictorially presented in Fig.1.

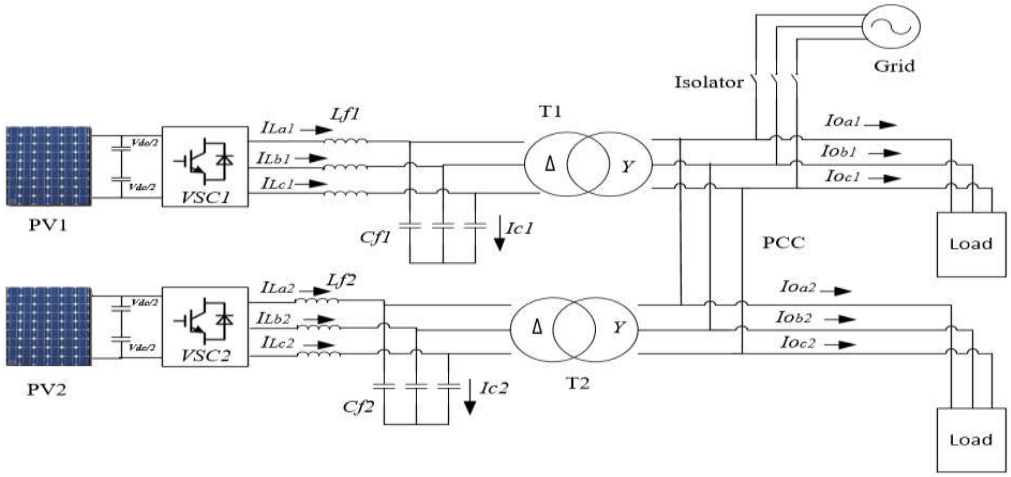

Figure 1. Schematic diagram of proposed microgrid.

Preprints (www.preprints.org) | NOT PEER-REVIEWED | Posted: 16 May 2022 doi:10.20944/preprints202205.0204.v1

The proposed model is simulated in MATLAB/Simulink. The dq-framed inner loop control is employed to individually regulate the real and reactive power at the PCC. Furthermore, the proposed model is analyzed and compared by employing a mathematical model of AC system dynamics, inner loop control, output voltage quality, AC harmonic spectrum analysis, and total harmonic distortion (THD) in both grid interconnected and island mode. The AC harmonic spectrum and THD are achieved in permissible range, in island mode.

3. DNN Based MPPT Controller for PV

The MPPT algorithm is critical for maximizing power output from renewable energy sources under a variety of weather conditions. Many researchers have designed the unique MPPT algorithm using the incremental drive, Fuzzy, ANN, P&O, PSO, ANFIS, feedback voltage/current, and other controllers during the past decade [22, 23]. In this study, an MPPT algorithm for a PV system is designed, employing a deep neural network controller (DNN) similar to [24]. In DNN learning algorithm, more than 80000 sample points are employed to train the MPPT algorithm. *Vdc** is the output voltage of the proposed DNN controller at which the PV module can produce maximum power. The DNN controller harnesses the optimum available power from PV arrays and gives the most efficient voltage *Vdc** (maximum power point).

Fig.2 shows the suggested DNN layer. The MPPT network is trained utilizing the input data (PV voltage, PV current) and target output is maximum power tracked dc voltages *Vdc**.

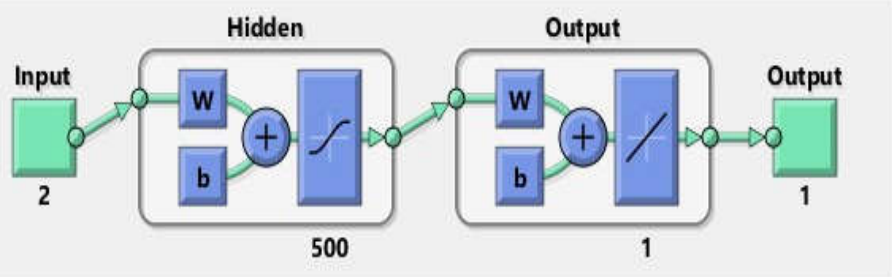

Figure 2. Proposed DNN layers.

In the DNN layer, there are a lot of input neurons, hidden-layer neurons, and an output neuron. The proposed DNN controller is considered the same analogous to classical MPPT based DC-DC converters in which MPPT controller gives duty cycle to the buck-boost converter (DC-DC) to produce *Vdc**. The flow chart of the proposed DNN is given in Fig.3. The proposed DNN controller's error histogram is depicted in Fig.4.

The hidden neuron can impact the error of the output nodes and error determines the stability of the neural network. As the error reduces, reliability is enhanced, and error is larger, stability becomes worse. The undesirable hidden neurons would overestimate the intricacy of the target query, resulting in over-fitting of the neural networks. The suggested DNN trained network gradient and validation check are shown in Fig.5.The mean square error is depicted in Fig.6. Finally, the suggested DNN based MPPT algorithm has been implemented, and Fig.7 shows the best regression for training data, test data, and overall performance data.

Preprints (www.preprints.org) | NOT PEER-REVIEWED | Posted: 16 May 2022 doi:10.20944/preprints202205.0204.v1

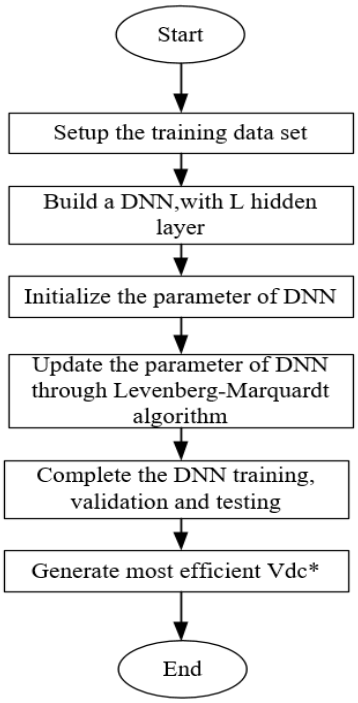

Figure 3. Flow chart of the Proposed DNN based MPPT Controller [24].

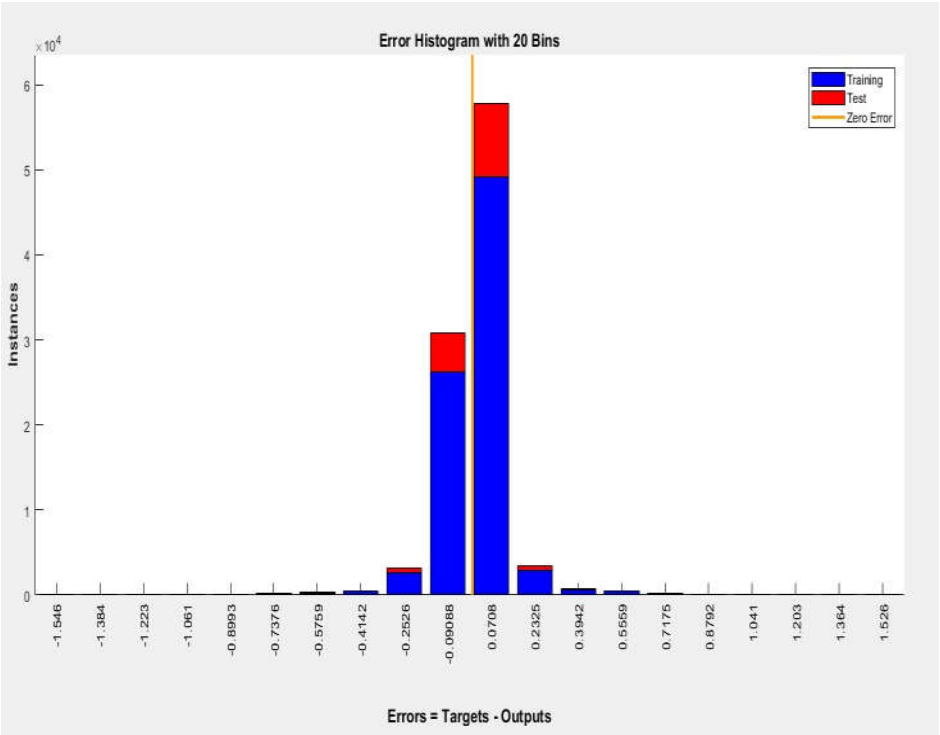

Figure 4. Proposed DNN based MPPT controller error histogram.

Preprints (www.preprints.org) | NOT PEER-REVIEWED | Posted: 16 May 2022 doi:10.20944/preprints202205.0204.v1

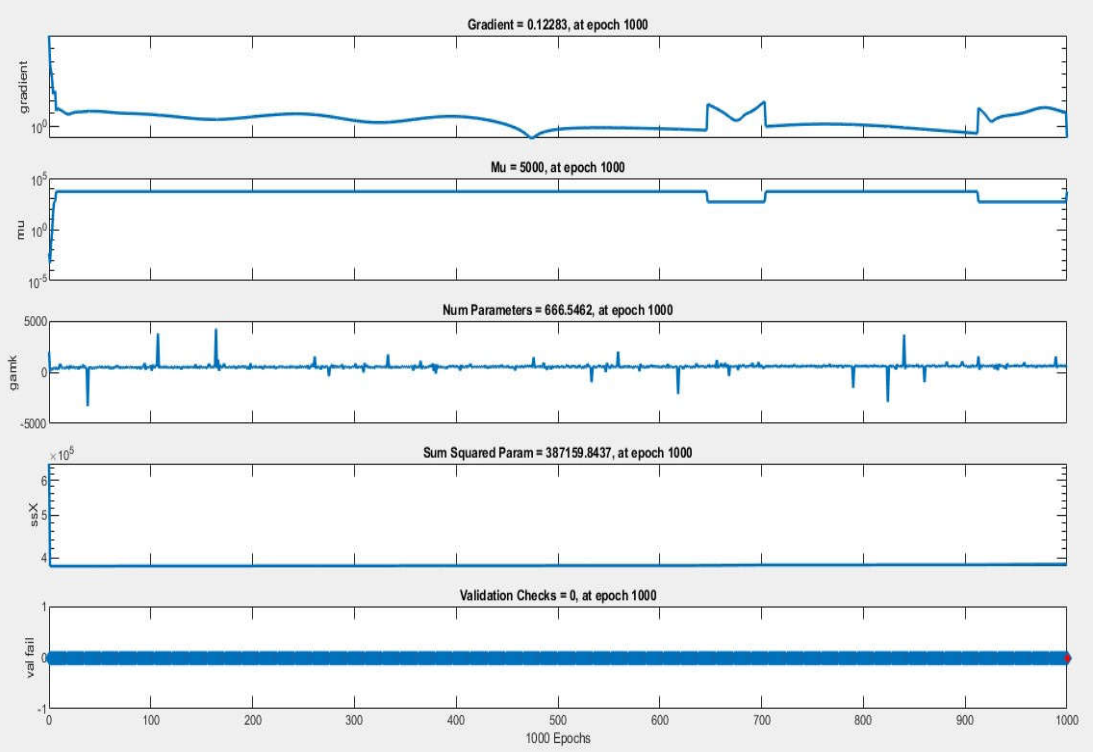

Figure 5. Proposed DNN based MPPT controller training data.

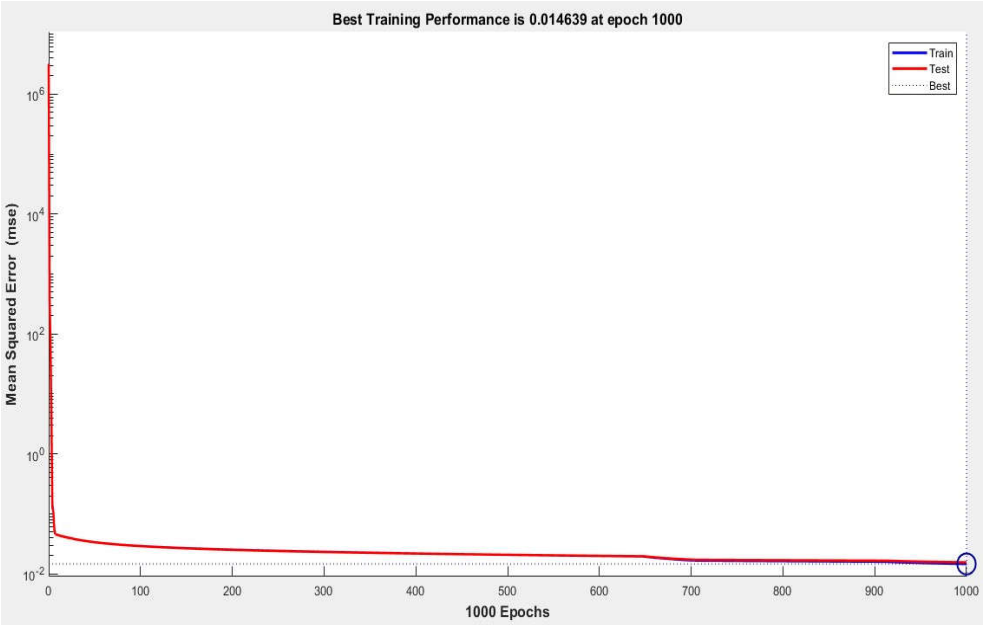

Figure 6. Proposed DNN based MPPT controller mean square error.

Preprints (www.preprints.org) | NOT PEER-REVIEWED | Posted: 16 May 2022 doi:10.20944/preprints202205.0204.v1

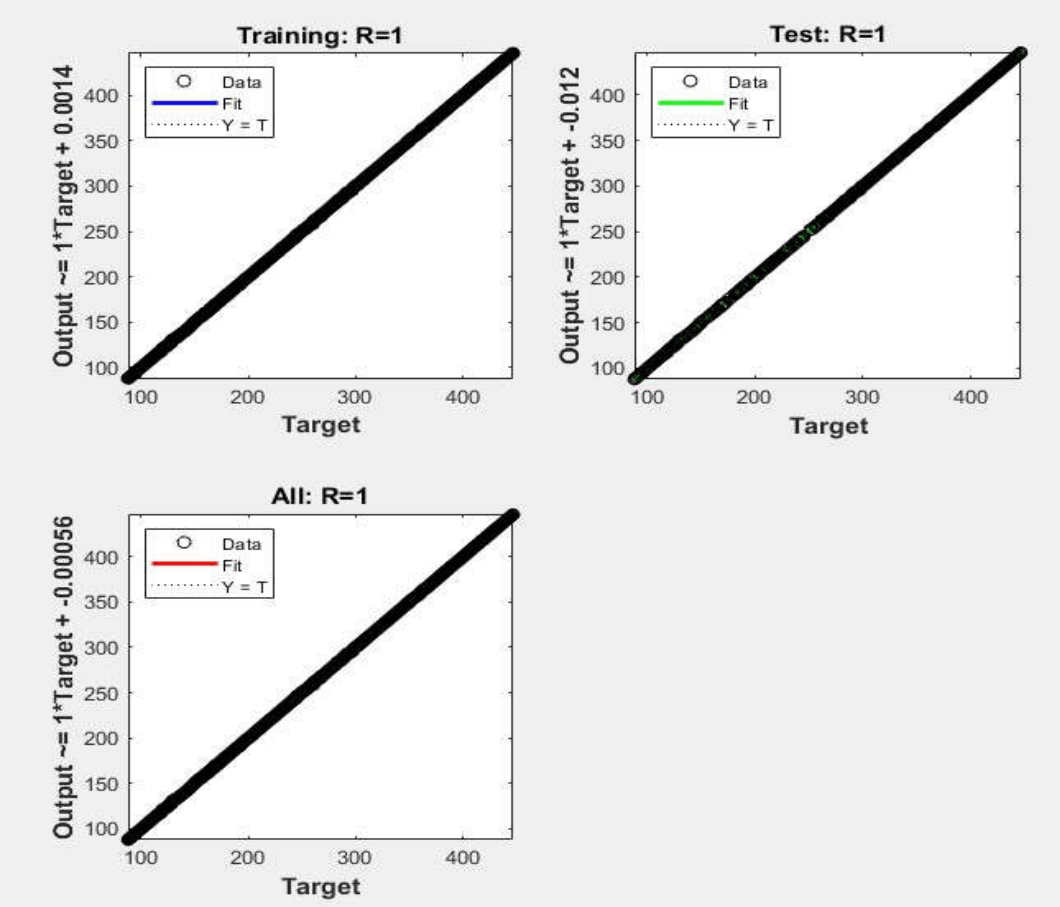

Figure 7. DNN-PV MPPT showing the best regression.

In the suggested simulation model and DNN-based methodology, 255.66kWp PV array is employed, with the target output being controlled Vdc*. More than 80,000 PV voltage and current data points are used to train the MPPT network. The DNN controller has been trained and its best output is presented in Fig.8. According to Fig.8, the DNN controller delivered Vdc* up to 480 Vdc for 0.33s when connected to the grid, and subsequently delivered Vdc* up to 550 Vdc in autonomous mode. Fig.9 and Fig.10 show the mean PV voltages, mean PV currents, and dc powers of both PV arrays, respectively.

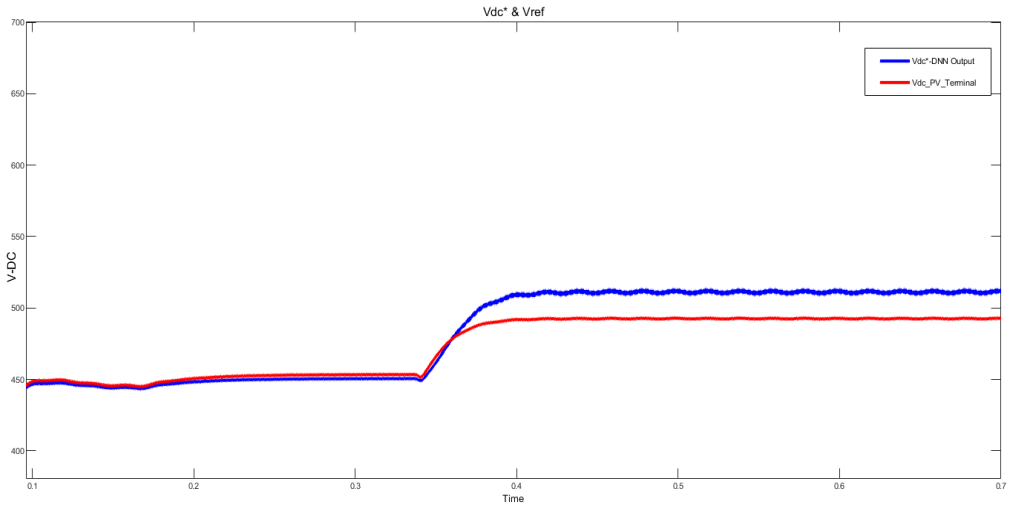

Figure 8. Proposed DNN controller output.

Preprints (www.preprints.org) | NOT PEER-REVIEWED | Posted: 16 May 2022 doi:10.20944/preprints202205.0204.v1

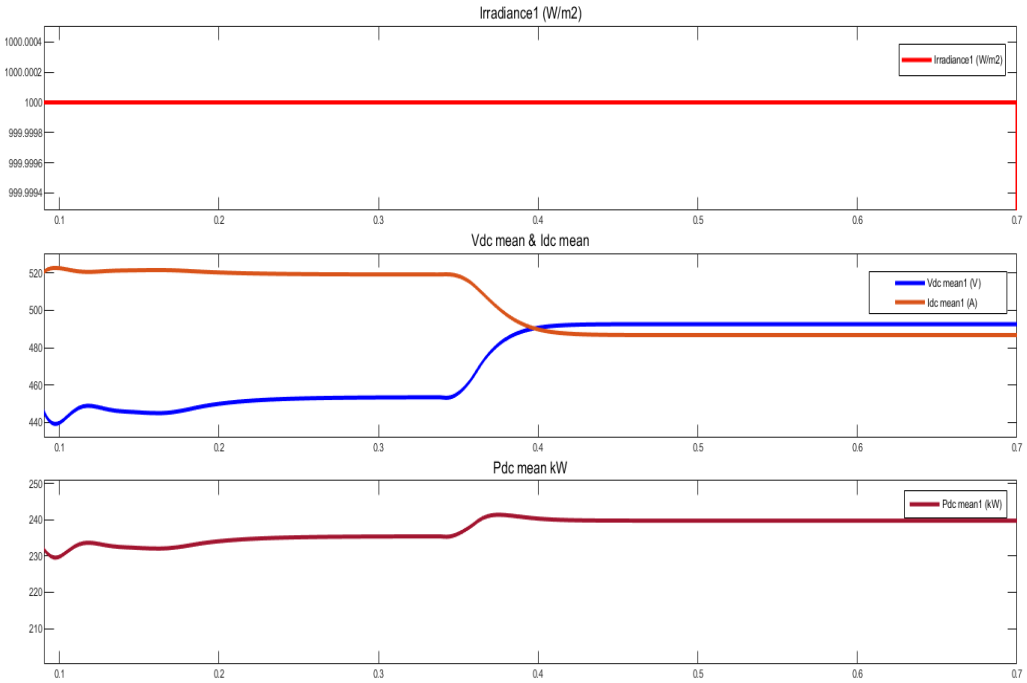

Figure 9. Irradiances, mean voltage, current and power of PV array 1.

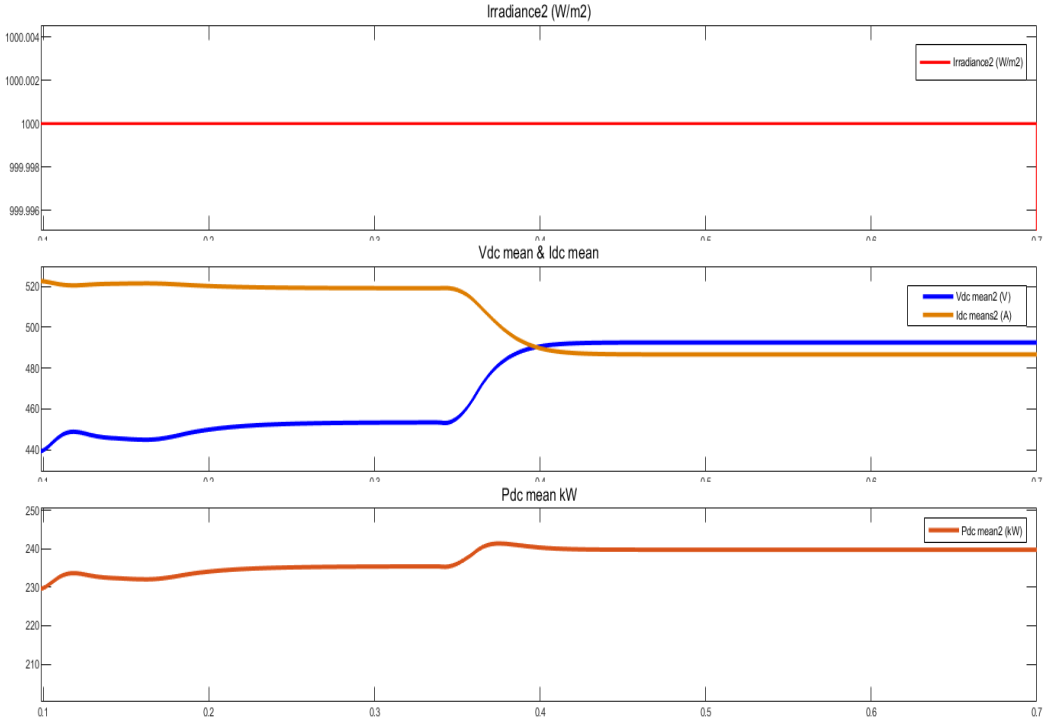

Figure 10. Irradiances, mean voltage, current and power of PV array 2.

4. Microgrid Control for Parallel Connected VSCs

The Matlab/Simulink model for microgrid based on grid interconnected and island mode is presented in Fig.11. The current effort presents a microgrid controller interfaced with DNN based MPPT controller and an inner current control loop based on SRF-PLL, as shown in Fig.12.Traditional feed forward PI regulators are used in the proposed controller, the inner control loop to provide high dynamic responsiveness.

Preprints (www.preprints.org) | NOT PEER-REVIEWED | Posted: 16 May 2022 doi:10.20944/preprints202205.0204.v1

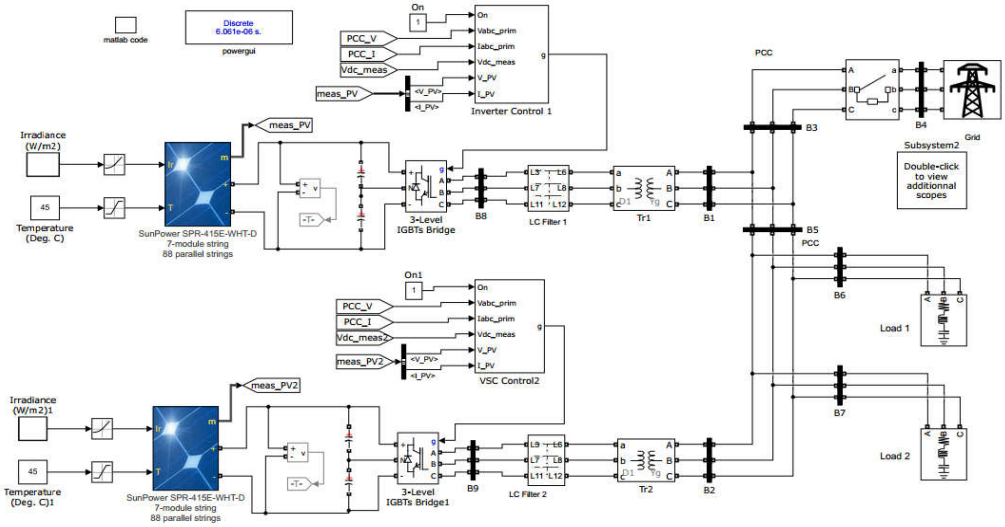

Figure 11. Simulation model of microgrid comprising of parallel operated VSCs.

The line current components *id* and *iq* regulate the active and reactive power [25].First, feedback and feedforward signals are converted into *dq*-frame and then the current controller compensator produced the control signal in the *dq*-frame. Control signals are subsequently transmitted to the VSC's SPWM system in the *abc*-frame [26]. As a result, if the load current, *Ioabc*, is disrupted, the control goal is to regulate the amplitude and frequency of the load voltage, *Vsabc*.

The LC filter functions as a low-impedance conduit for the VSC switching current harmonics, preventing them from permeating the load [27]. Without *Cf*, the switching frequency and its harmonics would have a large impact on the total harmonic distortion of the load voltage. The control diagram of VSC2 is analogous to VSC1, therefore only control of VSC1 is being addressed. The parameters selected for the Simulink model are presented in Table3 and Table 4.

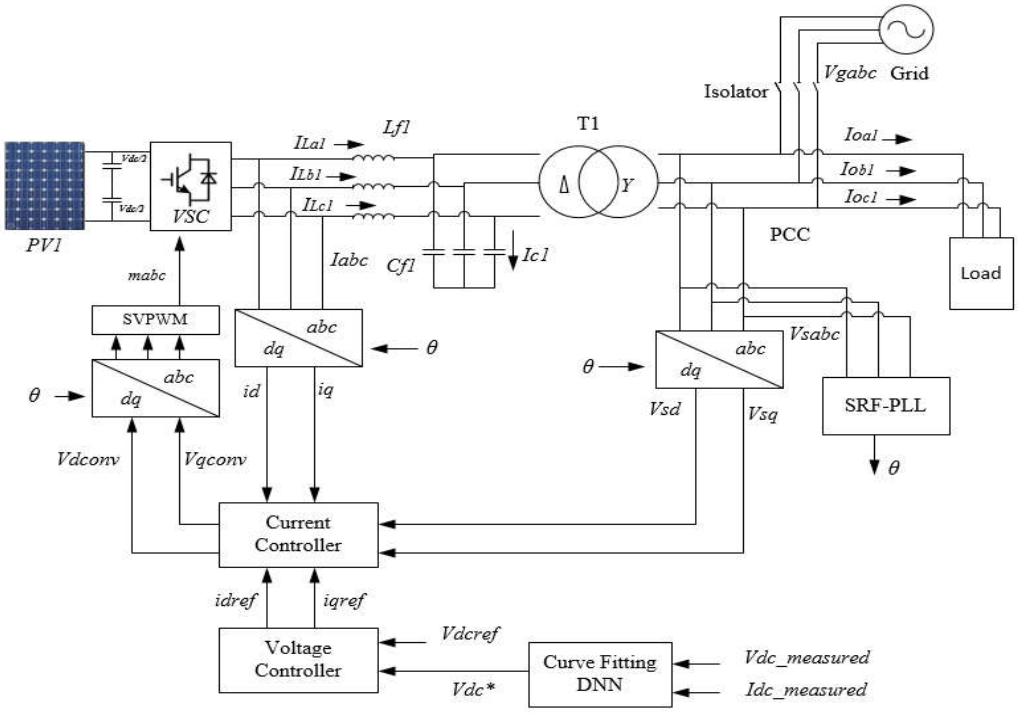

Figure 12. Proposed control diagram of VSC1.

Preprints (www.preprints.org) | NOT PEER-REVIEWED | Posted: 16 May 2022 doi:10.20944/preprints202205.0204.v1

The real and reactive power of the VSC denoted as follows [28, 29]:

$$Ps = \frac{3}{2}(vsd * id + vsq * iq) \quad (1)$$

$$Qs = \frac{3}{2}(vsd * id - vsq * iq) \quad (2)$$

where *Vsd* and *Vsq* are *dq*-coordinate of AC system voltages and *id* and *iq* are *dq*-coordinate of AC system current. Fig.13 depicts the suggested voltage controller.

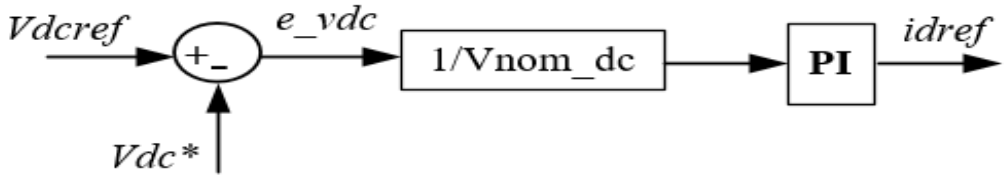

Figure 13. Proposed voltage controller.

$idref$ can be defined as follows[30]:

$$idref = \frac{1}{Vnom\_dc}(k_{p-Vdc} + k_{i-Vdc}\int (vdcref - Vdc^*)dt \quad (3)$$

where k_{p-Vdc} and k_{i-Vdc} are proportional and integral coefficients of PI controller respectively, in proposed voltage controller. These can be calculated as following [31]

$$k_{p-Vdc} = L/\tau_i \quad (4)$$

$$k_{i-Vdc} = R/\tau_i \quad (5)$$

Proposed current controller diagram can be seen in Fig.14.

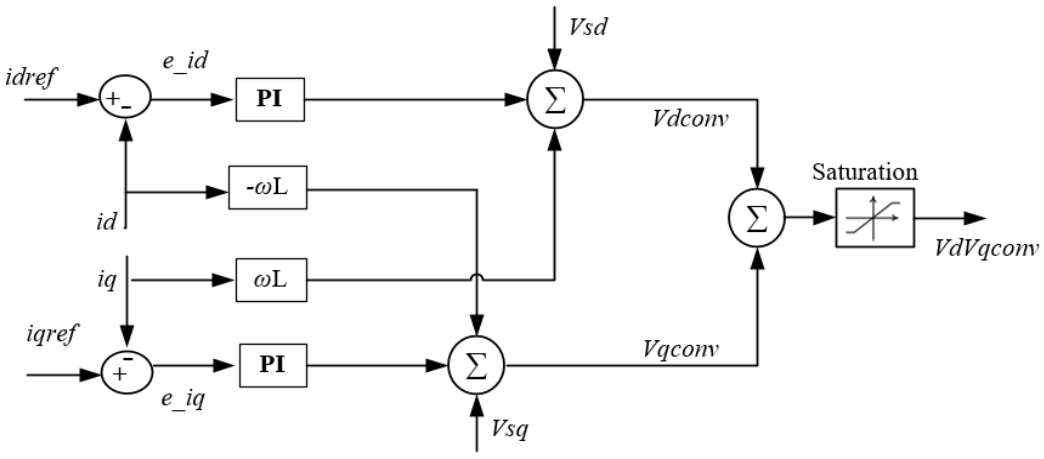

Figure 14. Proposed current controller.

In the dq-frame of SPWM, the reference voltage command signals to SPWM can be defined as follows [26]:

$$Vdconv = kp(idref - id) + ki\int (idref - id)dt - \omega LfIq + Vsd \quad (6)$$

$$Vqconv = kp(iqref - iq) + ki\int (iqref - iq)dt - \omega LfIq + Vsq \quad (7)$$

Preprints (www.preprints.org) | NOT PEER-REVIEWED | Posted: 16 May 2022 doi:10.20944/preprints202205.0204.v1

where *Vsd* and *Vsq* are *dq*-coordinate of AC system voltages and *id* and *iq* are *dq*-coordinate of AC system current respectively. k_p and k_i are proportional and integral coefficients of current PI controller. ω is the angular frequency, *idref* and *iqref* are reference inputs of *dq*-coordinate of current PI controller. These k_p and k_i can be selected as following[32]:

$$kp = k_{p-Ireg} = \frac{\tau_i * R}{2T_a} \tag{8}$$

$$ki = k_{i-Ireg} = \frac{kp}{\tau_i} \tag{9}$$

where $Ti = \tau_i$; $T_a = \frac{1}{fsw}$ Ti is the PI time constant, R is the damping resistor and fsw is the switching frequency.

VSC1 and VSC2 have analogous decentralized control, therefore only one VSC1 control is being addressed. A DNN based MPPT controller, voltage controller and current controller, SRF-PLL controller, and SPWM generating loop are included in the Simulink control model illustrated in Fig.15 for controlling active and reactive power.

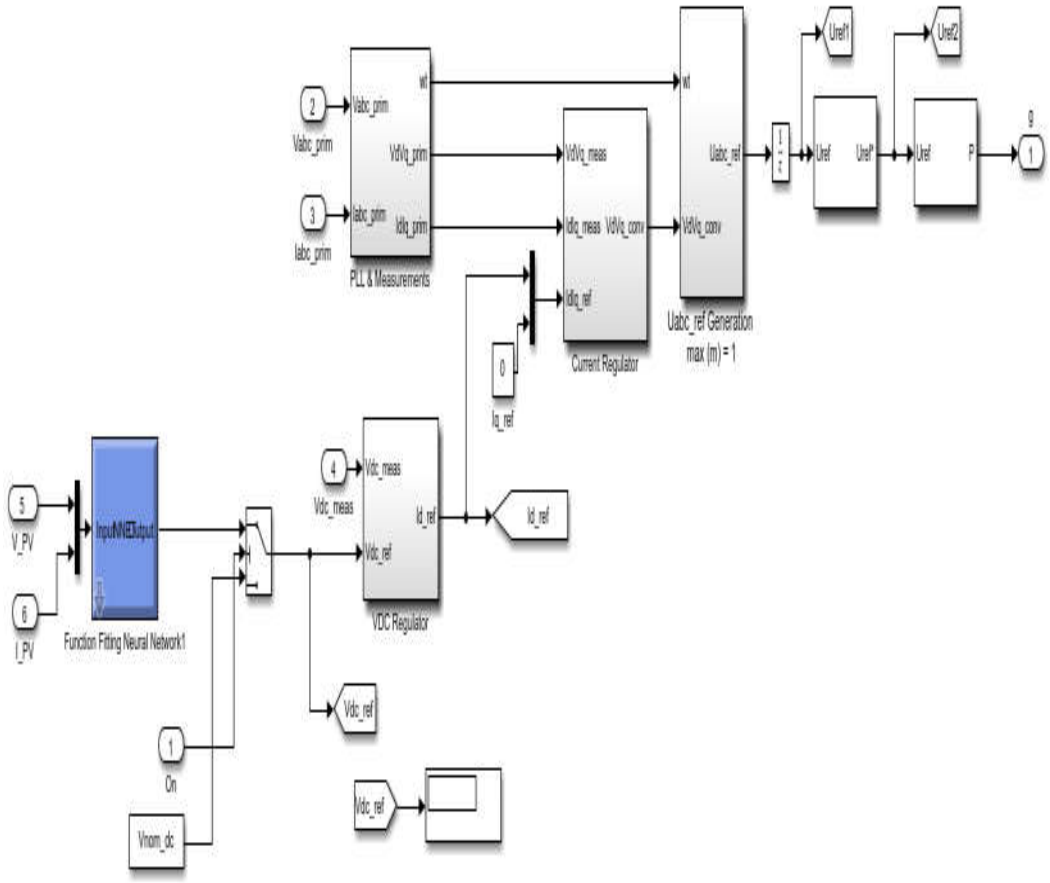

Figure 15. Simulink Model for VSC1 and VSC2 control.

Preprints (www.preprints.org) | NOT PEER-REVIEWED | Posted: 16 May 2022 doi:10.20944/preprints202205.0204.v1

Table 3. PI controllers parameters.

Description	Symbol	Values
k_{p-Ireg} of current PI controller	k_{p-Ireg}	0.608
k_{i-Ireg} of current PI controller	k_{i-Ireg}	6.08
k_{p-Vdc} of voltage PI controller	k_{p-Vdc}	2
k_{i-Vdc} of voltage PI controller	k_{i-Vdc}	200
k_{p-pll} of SRF-PLL PI controller	k_{p-pll}	50
k_{i-pll} of SRF-LL PI controller	k_{i-Ireg}	650
Sampling Time for GUI	T_{s_Power}	$6.06e^{-06}\ s$
Sample Time of PI controllers	$T_{s\_Control}$	$6.061e^{-05}\ s$
Feedforward values of current controller	$RLff(1)$	0.039 pu
Feedforward values of current controller	$RLff(2)$	0.210 pu

Table 4. Specification of Simulink Model.

Description	Symbol	Values
Fundamental frequency	f	$50\ Hz$
PCC/Primary voltage	V_{nom_prim}=V_{sabc}	$11k\ V$
VSCs output voltage	V_{nom_sec}	$415\ V$
AC grid voltages	V_{gabc}	$11k\ V$
Sampling Time for GUI	T_{s_Power}	$6.06e^{-06}\ s$
Sampling frequency	f_s	$165000\ Hz$
Line Inductor	Lf	$0.748mH$
Line Capacitor	Cf	$220\mu F$
Transformers Tr1 and Tr2		
Nominal power	P_{nom}	$280\ kVA$
Primary voltage	V_{nom_prim}	$11k\ V$
Secondary voltage	V_{nom_sec}	$415\ V$
Load 1 and Load2		
Active power	P_{Load1}, P_{Load2}	$220\ , 200\ kW$
Inductive Reactive power	Q_{L1}, Q_{L2}	$10\ , 20\ VAR$
Capacitive Reactive power	Q_{C1}, Q_{C2}	$20\ \ \ , 10\ VAR$

4.1. SRF-PLL

The phase angle is followed by applying the Clarke transformation to convert the three phases of the voltage signals Vsa, Vsb, and Vsc to the two phases of the stationary system Vα and Vβ, as illustrated in Fig.16.The Park transformation converts the two-axis stationary reference frame $V\alpha$ and $V\beta$ into a rotating or synchronous reference frame [33].

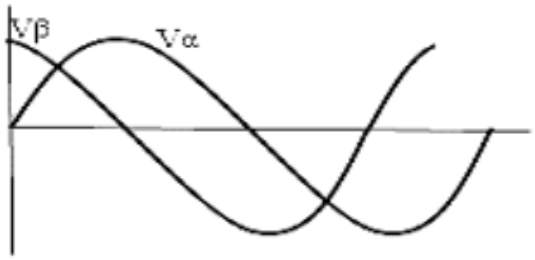

Figure 16. Clark Transformation.

Preprints (www.preprints.org) | NOT PEER-REVIEWED | Posted: 16 May 2022 doi:10.20944/preprints202205.0204.v1

The AC side voltages are given as

$$\boldsymbol{Vsabc} = \begin{bmatrix} Vsa \\ Vsb \\ Vsc \end{bmatrix} = V \begin{bmatrix} cos\ (\omega t\ +\ \delta) \\ \cos\left(\omega t + \delta - \frac{2\pi}{3}\right) \\ \cos\left(\omega t + \delta - \frac{4\pi}{3}\right) \end{bmatrix} \tag{10}$$

The $\alpha\beta$-transformation matrix by Clarke's Transformation is [34, 35]

$$\boldsymbol{V\alpha\beta} = [\boldsymbol{T_{\alpha\beta}}] \cdot \boldsymbol{Vsabc} \tag{11}$$

where $[\boldsymbol{T_{\alpha\beta}}]$ is Clark's Transformation matrix.

$$\begin{bmatrix} V\alpha \\ V\beta \end{bmatrix} = \frac{2}{3} \begin{bmatrix} 1 & -\frac{1}{2} & -\frac{1}{2} \\ 0 & \frac{-\sqrt{3}}{2} & \frac{\sqrt{3}}{2} \end{bmatrix} \begin{bmatrix} Vsa \\ Vsb \\ Vsc \end{bmatrix} \tag{12}$$

$$\begin{bmatrix} V\alpha \\ V\beta \end{bmatrix} = Vm \begin{bmatrix} \sin(\theta) \\ \cos(\theta) \end{bmatrix} \tag{13}$$

The $\alpha\beta$-reference frame is referred as the stationary reference frame. Fig.17 shows the two signal carrying the information of phase angle of one of two phases.

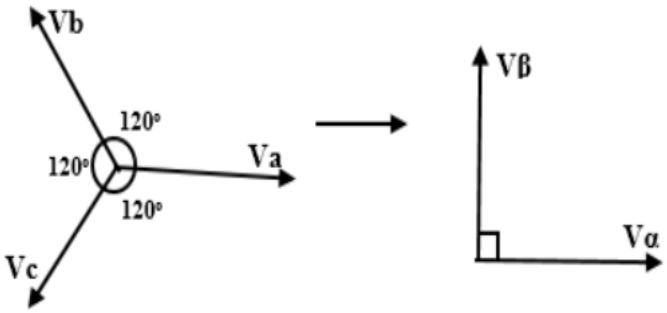

Figure 17. Two phase reference signal.

The dq-transformation matrix yield by Park's Transformation is [34, 35]

$$\boldsymbol{Vdq} = [\boldsymbol{T_{dq}}] \cdot \boldsymbol{V\alpha\beta} \tag{14}$$

where $[\boldsymbol{T_{dq}}]$ is Parks's Transforation matrix. The stationary reference frame voltages $V\alpha$ and $V\beta$are then converted into the synchronous reference frame as shown in Fig.18 using[36]

$$\begin{bmatrix} Vd \\ Vq \end{bmatrix} = \begin{bmatrix} \cos(\theta') & -\sin(\theta') \\ \sin(\theta') & \sin(\theta') \end{bmatrix} \begin{bmatrix} V\alpha \\ V\beta \end{bmatrix} \tag{15}$$

where θ' is estimated phase angle given by the SRF-PLL [36]

$$\begin{bmatrix} V\alpha \\ V\beta \end{bmatrix} = Vm \begin{bmatrix} \sin(\theta' - \theta) \\ \cos(\theta' - \theta) \end{bmatrix} \tag{16}$$

The phase error$(\theta' - \theta)$is negligible in steady state and the sine term is approximated as

$$Vd = Vmsin(\theta' - \theta)\ \approx Vd = Vm(\theta' - \theta) \tag{17}$$

Preprints (www.preprints.org) | NOT PEER-REVIEWED | Posted: 16 May 2022 doi:10.20944/preprints202205.0204.v1

The above equations are used to implement linearized model of SRF-PLL as illustrated in Fig.19.

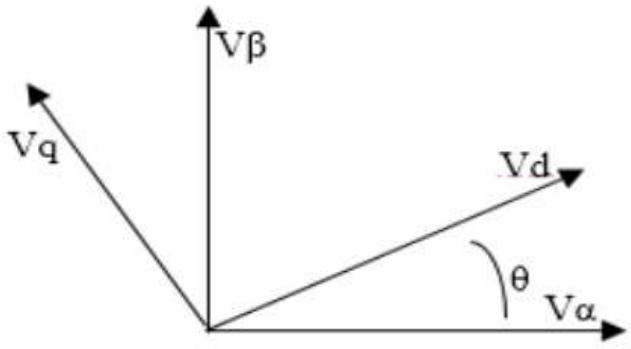

Figure 18. Park's Transformation.

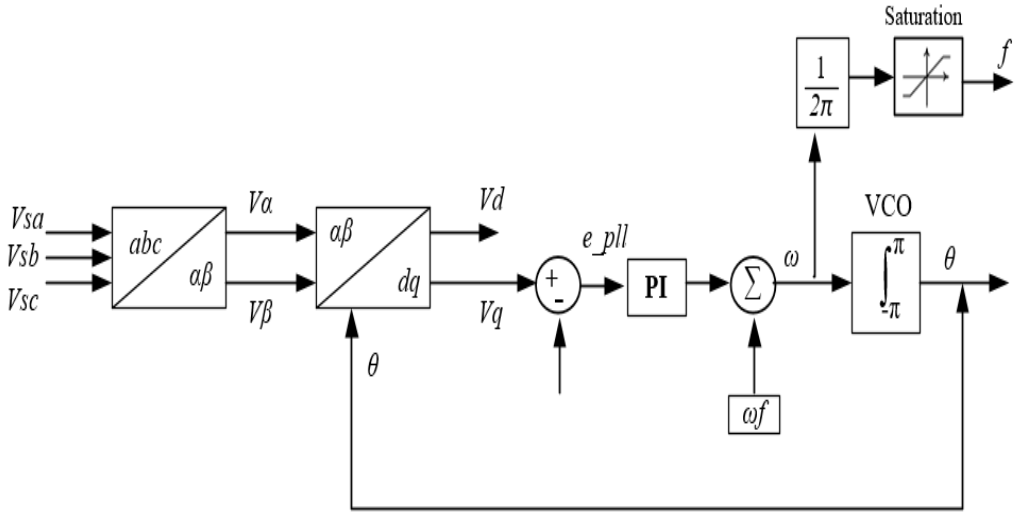

Figure 19. The proposed linearized model of SRF-PLL.

θ is the phase angle of VSC output voltage and e_pll is angular frequency error generated by loop filter of SRF-PLL can be calculated as [37]

$$\theta(t) = \theta_{ref}(t) = \int (\omega_{nom} - e\_pll)dt \quad (18)$$

$$e\_pll = -(k_{p-pll} * V_q + k_{i-pll} * (V_q)\, dt \quad (19)$$

k_{p-pll} and k_{i-pll} are proportional and integral coefficients of SRF-PLL PI controller.

SRF-PLL is used to compute the phase angle of grid voltage. Grid angle is computed using the grid's q-component, with the reference angle value set to zero [38]. The PI regulator receives the angle error and creates an angular frequency. The true angular frequency is calculated by adding the PI output signal to the basic angular frequency of grid voltage.

The angular frequency is integrated to produce the instantaneous phase angle. The phase angle can be determined by synchronizing the voltage vector along the d-axis [36].The three-phase SRF-PLL is less susceptible to power quality problems including harmonics, voltage unbalance, sag, and the swell case [30].The SRF-PLL Simulink model as shown in Fig.20 is built using the mathematical modeling described in eq. (11) to (19).

Preprints (www.preprints.org) | NOT PEER-REVIEWED | Posted: 16 May 2022 doi:10.20944/preprints202205.0204.v1

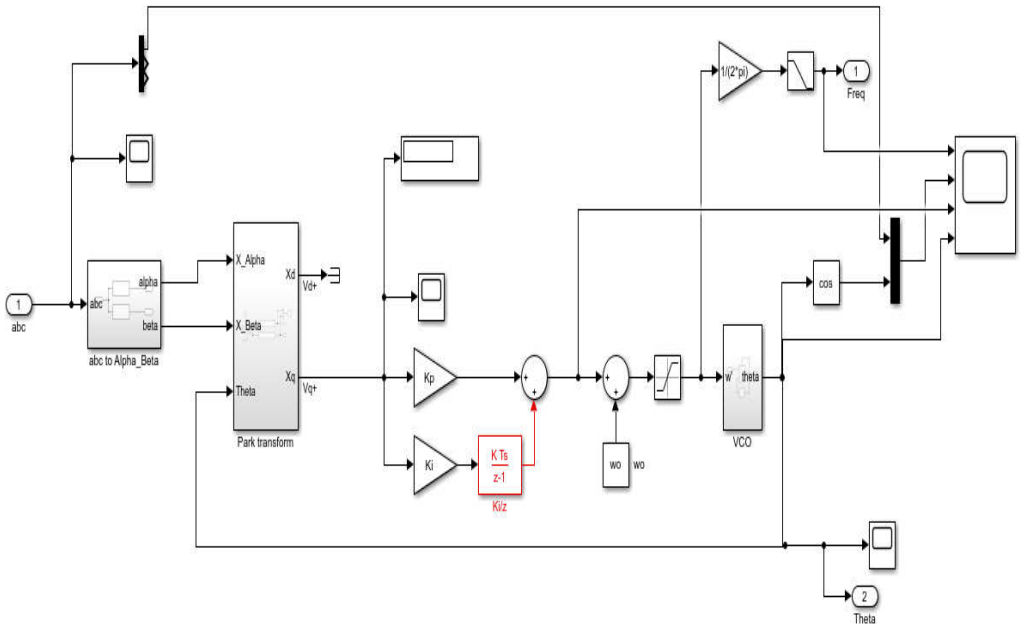

Figure 20. Simulink Model for SRF-PLL.

5. Results and Discussions

In the Simulink model, $11kV$, $50Hz$ AC grid is interfaced with two parallel-connected VSCs through LC filters and the coupling transformers. Two PV sources of 255.66 kWp are employed to give full dc-link voltages at the input of converters. The LC filters are used to provide the interface between VSCs and transformers. As illustrated in Fig.11, the Simulink model analyzes line voltages and currents using three-phase measurement. The Simulink model is simulated for 0.7s and the system is in grid-tied mode until 0.33s and then switched to autonomous mode till 0.7s. Since VSCs are connected in parallel at PCC and deliver power to the loads at PCC. Fig.21represents the voltages and currents waveforms at PCC.

The magnitude of the voltage at the PCC bus is same as of VSC1 and VSC2. The peak to peak voltage V_{p-p} is 31.11 kV and peak voltage V_p is 15.56kV. The three-phase line-to-line rms voltage V_{rms} is $11kV$ can be seen in Fig.24.The magnified view of PCC voltage and current waveforms in autonomous mode can be seen in Fig.22.When VSCs switch from grid to island mode, as demonstrated in Fig.23, a smooth and seamless transition is achieved. The magnitude of the current waveform is higher in grid-connected mode than autonomous mode as grid, VSC1 and VSC2 shared the current at PCC bus and drawn by the load1 and load2. Whearas, in autonomous mode both VSC1 and VSC2 shared the current equally and can be seen in Fig.25 and Fig.26.

Preprints (www.preprints.org) | NOT PEER-REVIEWED | Posted: 16 May 2022 doi:10.20944/preprints202205.0204.v1

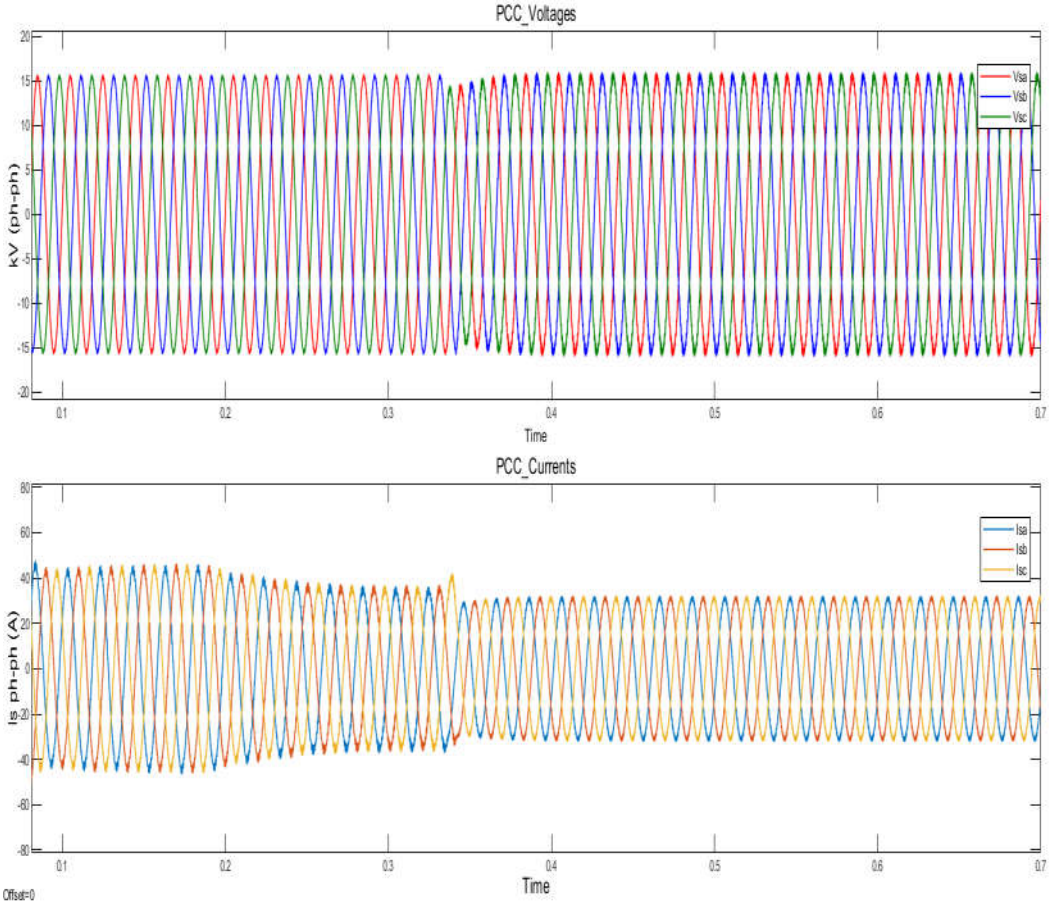

Figure 21. Three phase voltage and current waveforms at PCC bus.

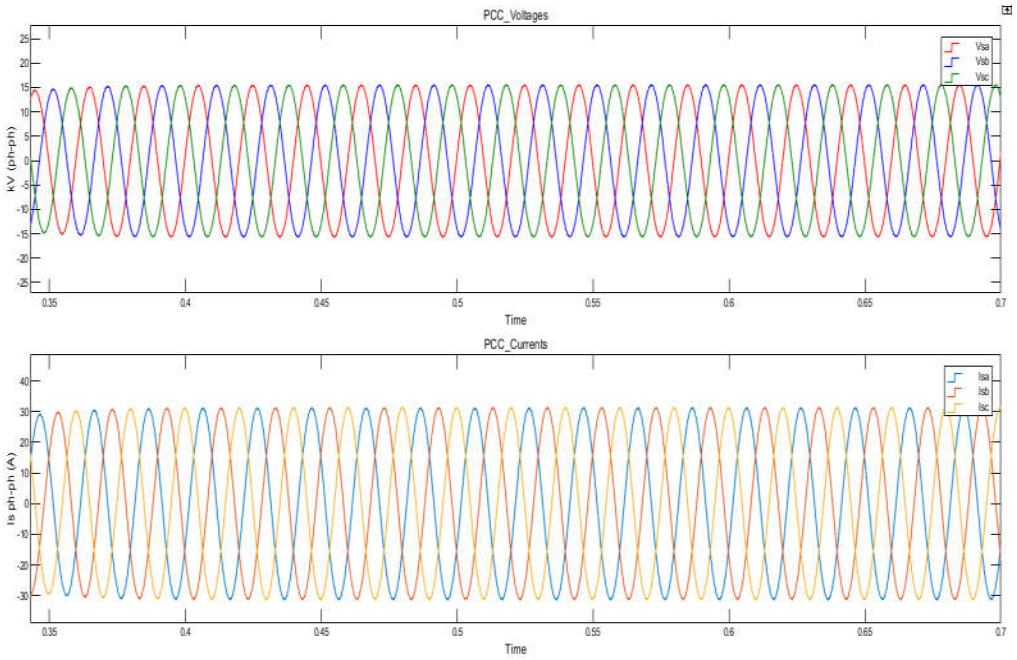

Figure 22. Magnified PCC bus voltage and current waveform in autonomous mode.

Preprints (www.preprints.org) | NOT PEER-REVIEWED | Posted: 16 May 2022 doi:10.20944/preprints202205.0204.v1

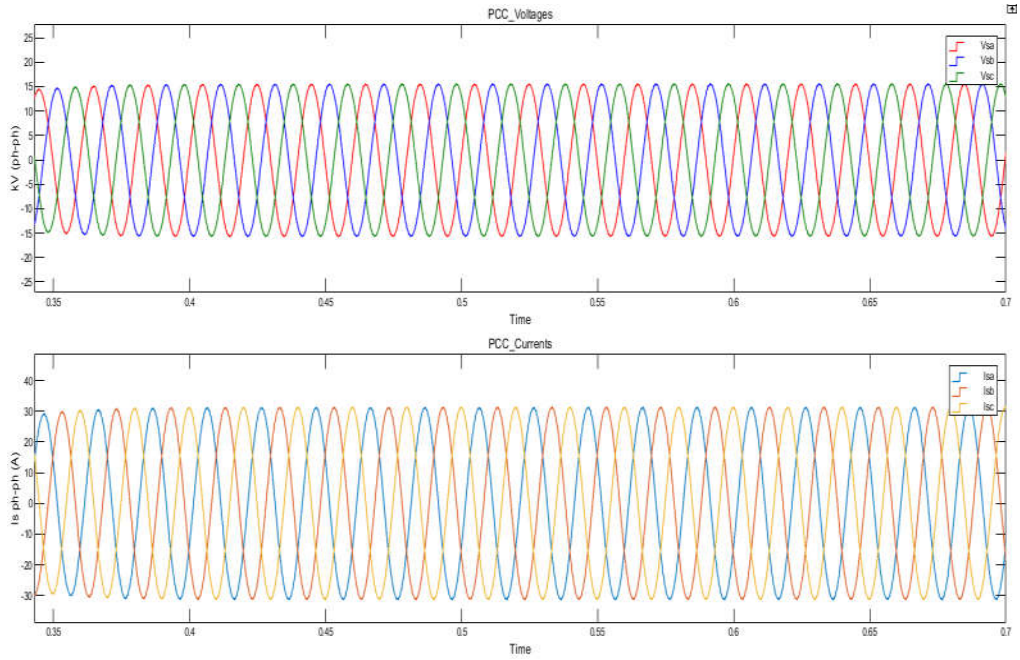

Fig. 22. Magnified PCC bus voltage and current waveform in autonomous mode.

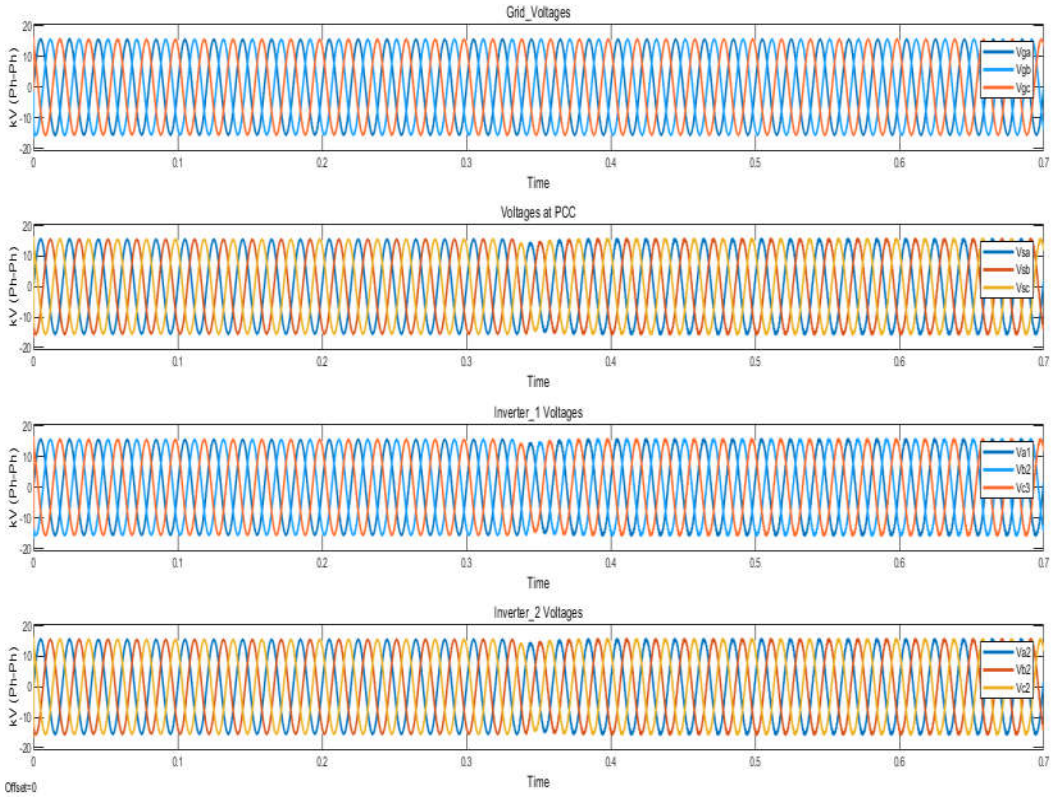

Figure 23. Voltage waveforms of grid, PCC,VSC1 and VSC2.

Preprints (www.preprints.org) | NOT PEER-REVIEWED | Posted: 16 May 2022 doi:10.20944/preprints202205.0204.v1

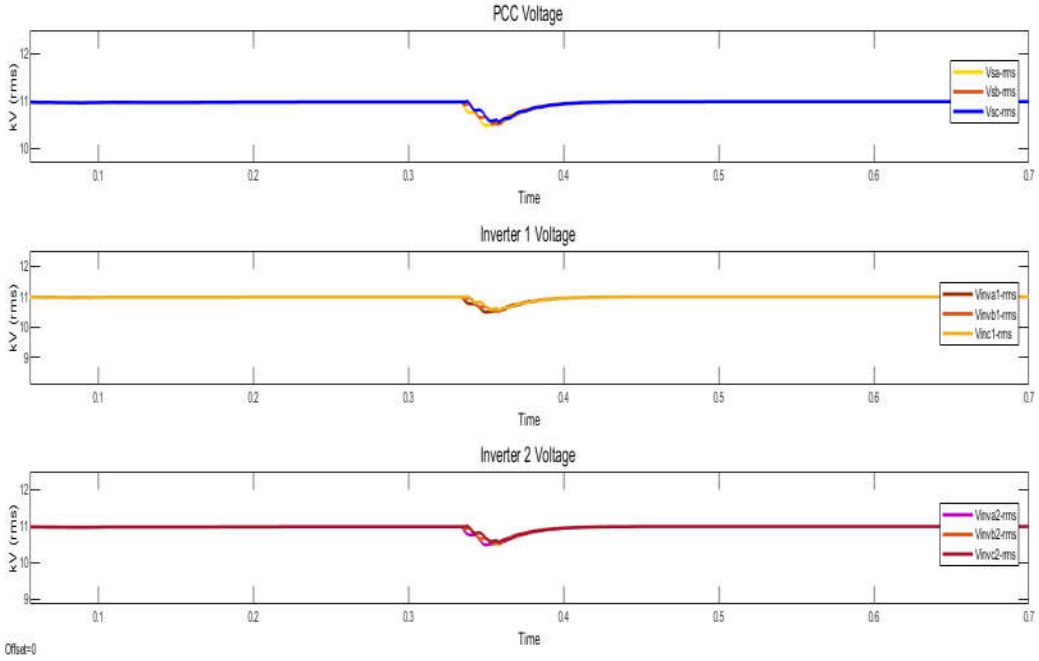

Figure 24. Rms voltage of parallel-connected VSC1, VSC2 and PCC.

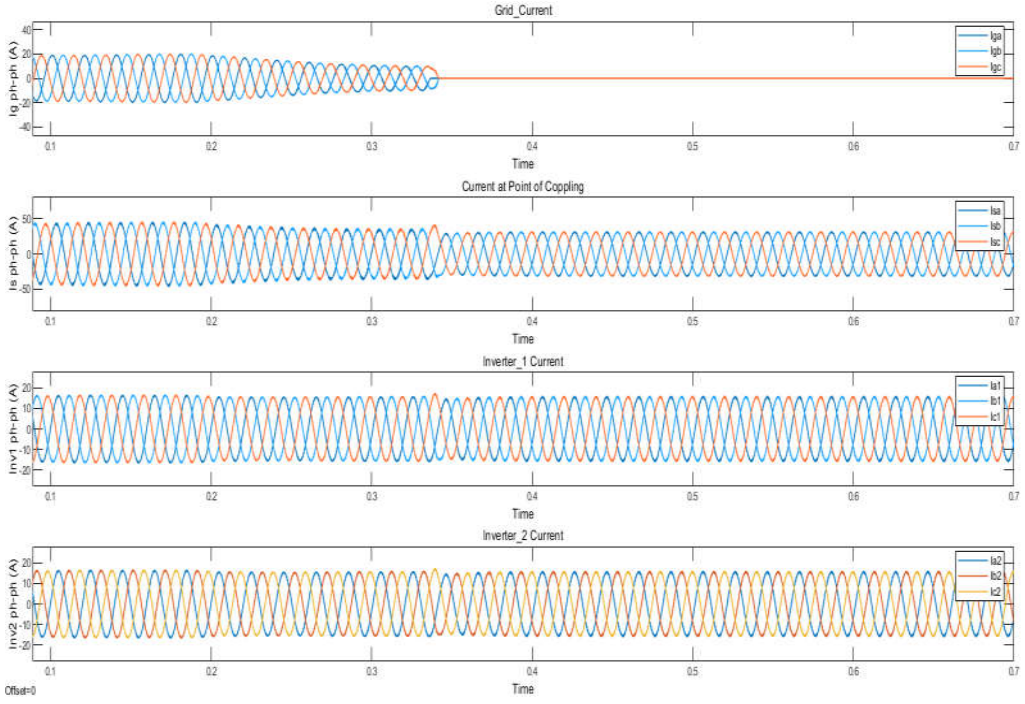

Figure 25. Current waveforms of grid, PCC, VSC1 and VSC2.

Preprints (www.preprints.org) | NOT PEER-REVIEWED | Posted: 16 May 2022 doi:10.20944/preprints202205.0204.v1

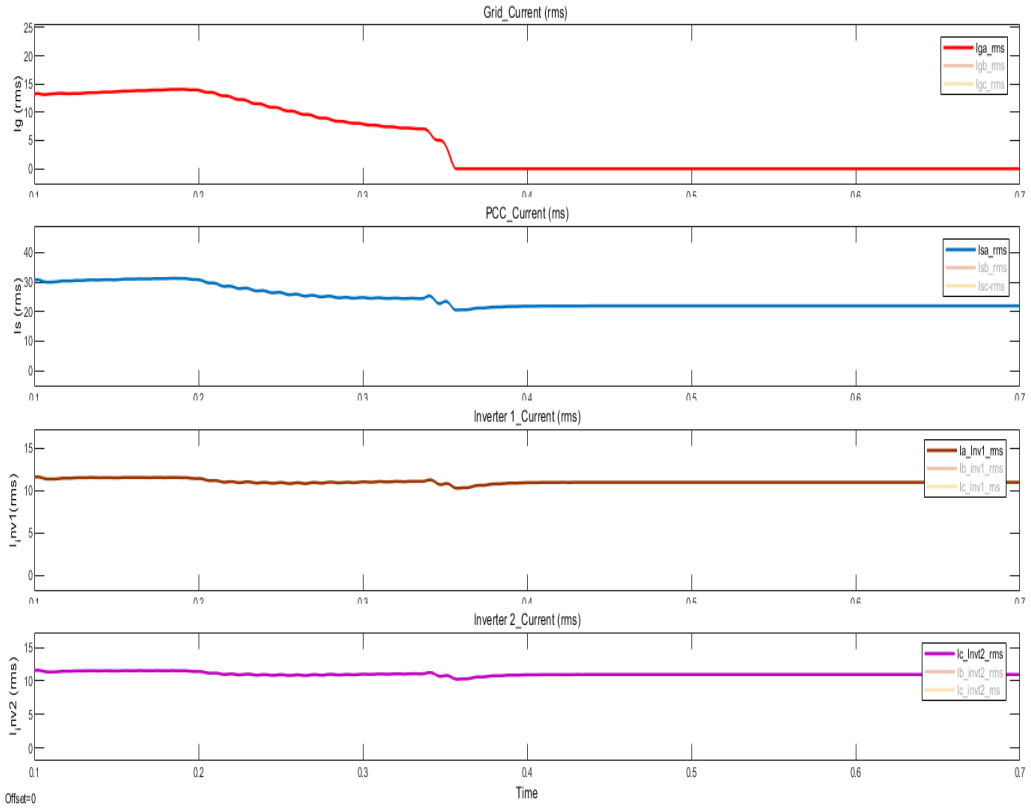

Figure 26. Rms value of phase A currents, of grid, PCC, VSC1 and VSC2.

The Simulink model for parallel-connected VSCs is analyzed based on the performance of SRF-PLL. It is analyzed that $cos(\theta)$ and Vsa (phase A of PCC voltage) are in phase and SRF-PLL tracked the theta reference properly. Fig.27 shows that frequency $50Hz$ remained constant during the transition of operation mode. The SRF-PLL1output of VSC1 is depicted in Fig.28. The magnified output of the SRF-PLL1 can be better seen in Fig.28.

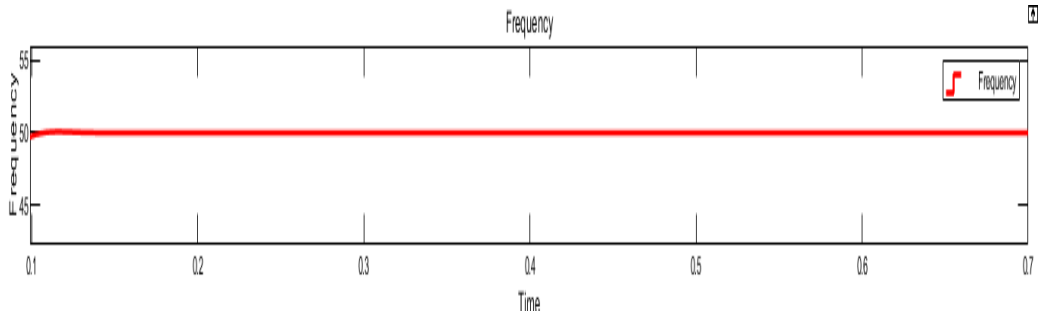

Figure 27. Frequency of microgrid.

Preprints (www.preprints.org) | NOT PEER-REVIEWED | Posted: 16 May 2022 doi:10.20944/preprints202205.0204.v1

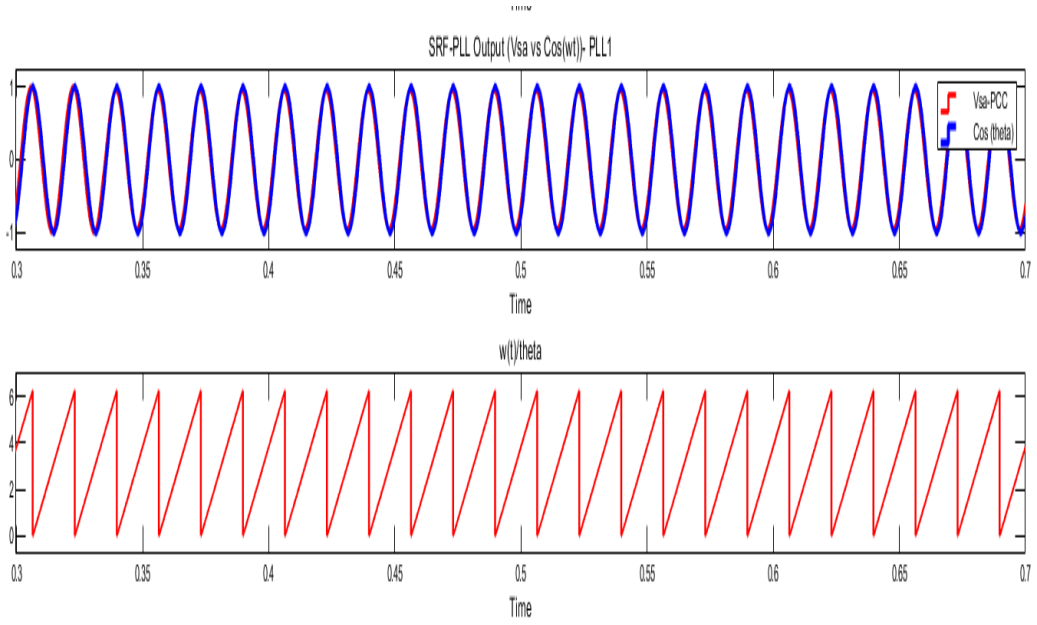

Figure 28. SRF-PLL output of VSC1.

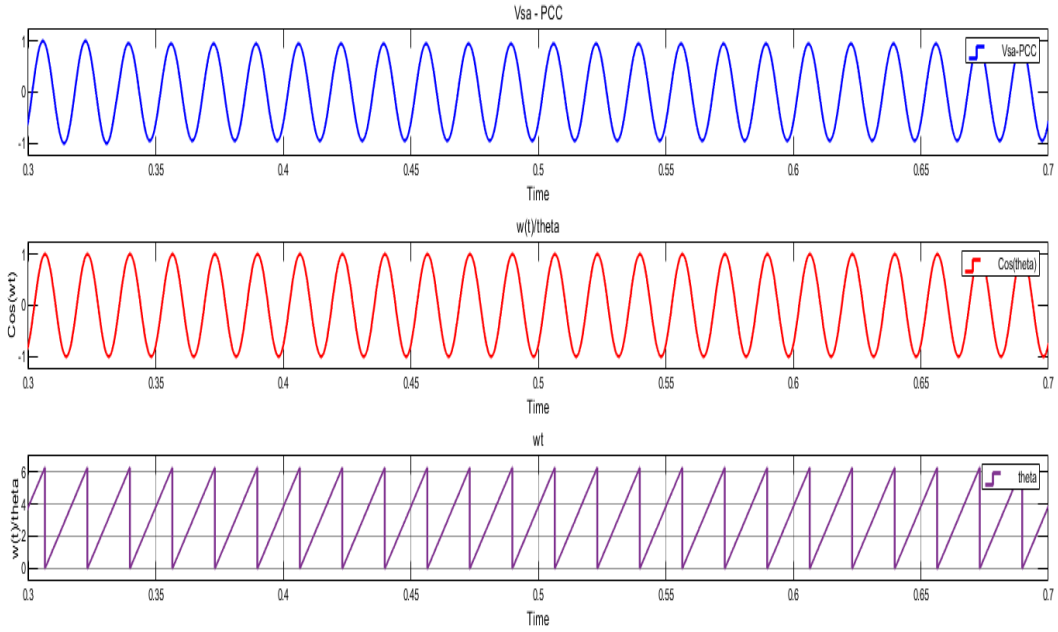

Figure 29. A magnified view of SRF PLL1 output.

The PCC voltage and current harmonic are also analyzed using the FFT analysis toolbox. The harmonic spectrum of PCC voltage and currents are presented in Fig.30 to Fig.31 in autonomous modes only.

Preprints (www.preprints.org) | NOT PEER-REVIEWED | Posted: 16 May 2022 doi:10.20944/preprints202205.0204.v1

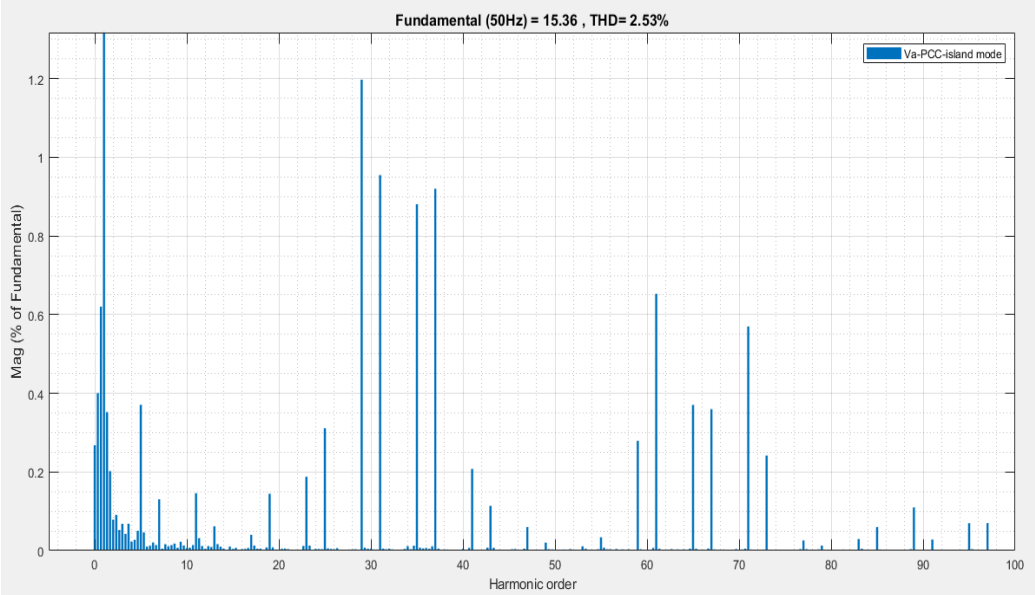

Figure 30. Harmonic spectrum of PCC voltage in autonomous mode.

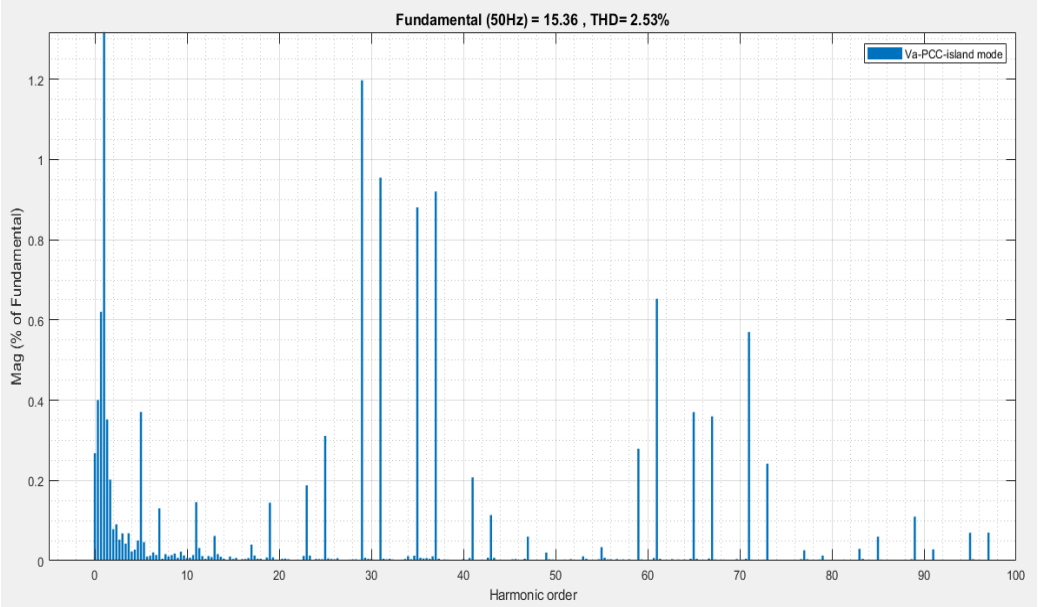

Figure 31. Harmonic spectrum of PCC current in autonomous mode.

According to IEEE standard 519™-2014[39] in Table 5, the amplitude of no single harmonic is larger than 3% in Fig.30 and Fig.31and both THD are within the permitted range, i.e. < 5%.The instantaneous real and reactive power of VSC1 and VSC2 is represented in Fig.32 and Fig.33, respectively. The Fig.34 represents the grid instantaneous active and reactive power.

Preprints (www.preprints.org) | NOT PEER-REVIEWED | Posted: 16 May 2022 doi:10.20944/preprints202205.0204.v1

Table 5. IEEE Standard 519TM-2014 [39].

PCC Bus Voltage	Single Harmonic	THD
$V \leq 1.0kV$	5.0%	8%
$1kV \leq V \leq 69kV$	3.0%	5.0%
$69kV \leq V \leq 161kV$	1.5%	2.5%
$161kV \leq V$	1%	1.5%

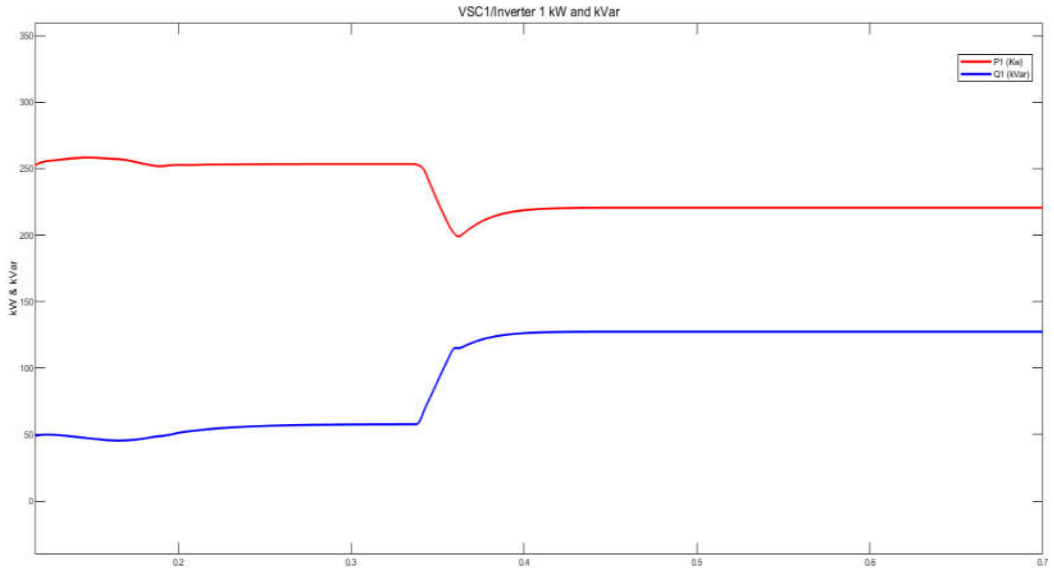

Figure 32. Real and reactive power of VSC1.

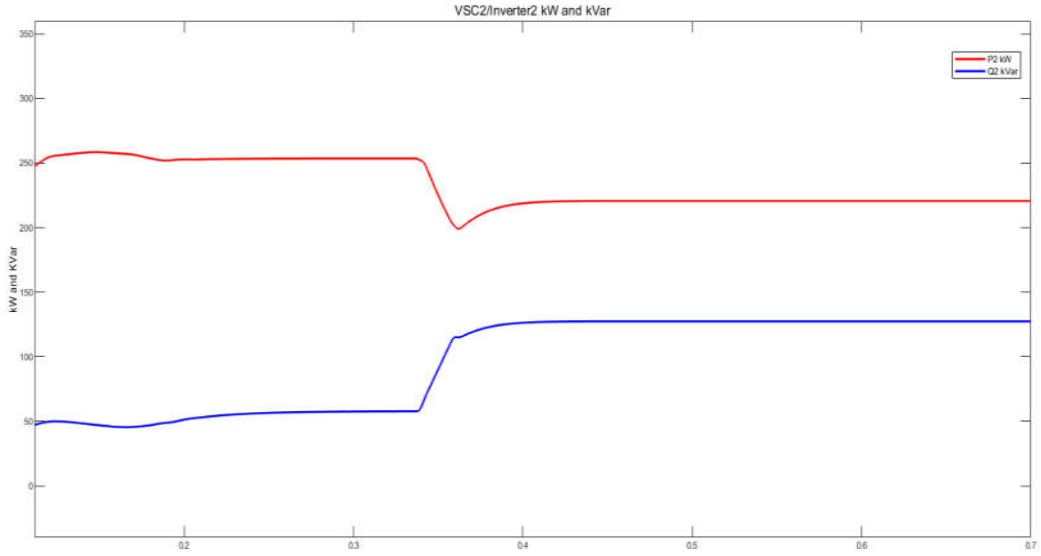

Figure 33. Real and reactive power of VSC2.

Preprints (www.preprints.org) | NOT PEER-REVIEWED | Posted: 16 May 2022 doi:10.20944/preprints202205.0204.v1

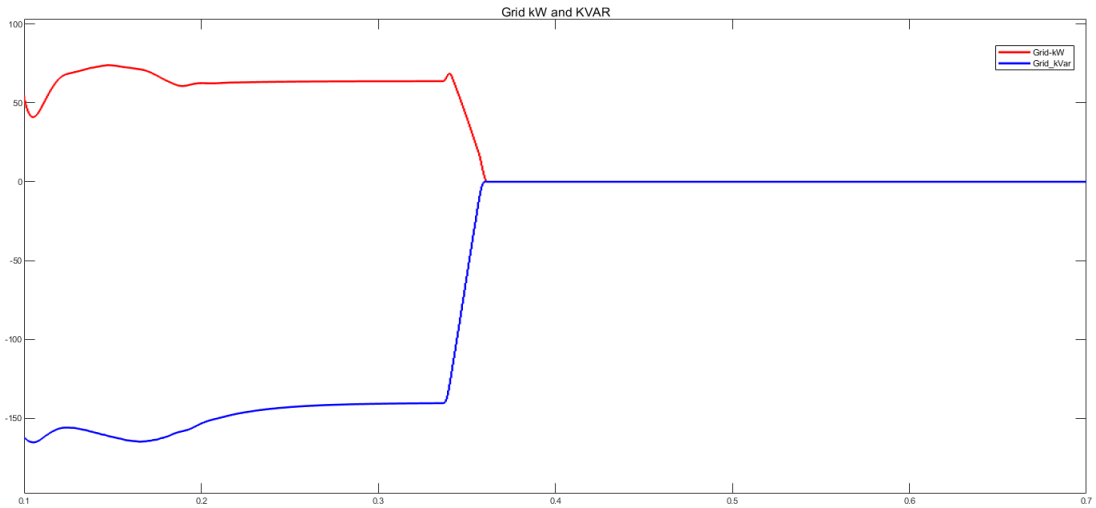

Figure 34. Real and reactive power of grid.

It is determined that in grid-tied mode, the grid absorbs reactive power and supplies active power to VSCs and loads. Additionally, more current is drawn from the grid in order to feed the converters as well as each load at its rated capacity. It may be read as follows: in grid-connected mode, VSCs function as load and supply reactive power to the grid. In autonomous mode, VSCs serve as a source, supplying real and reactive power to the loads only. Fig.35 depicts the power factor of the system i.e. 0.8667.

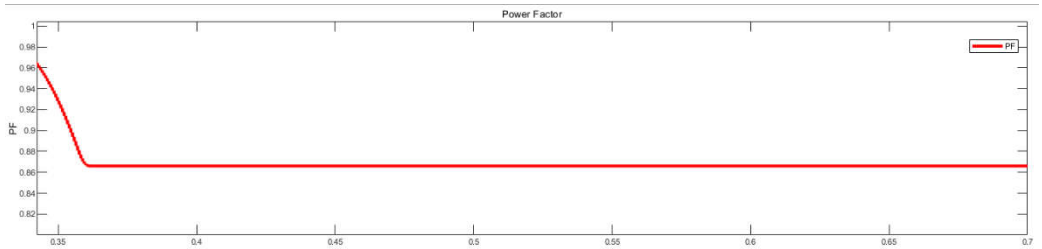

Figure 35. Power factor of microgrid.

To improve the power factor, the fixed capacitor bank $Qc \leq 15\%$ of transformer kVA i.e. 40kVAR is employed at PCC and the Simulink model is simulated for 0.7s. It is analyzed that after deploying capacitor bank at PCC, the power factor increased from 0.8667 to 0.9091 as shown in Fig.36.

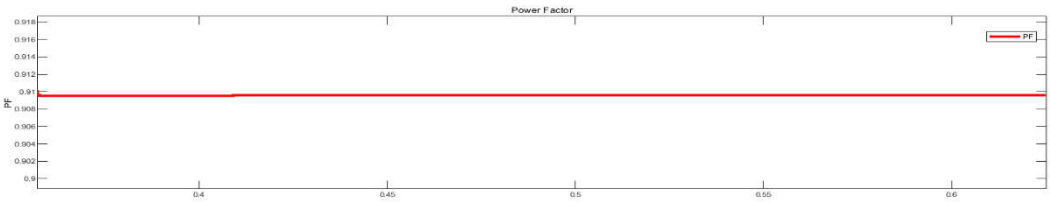

Figure 36. Improved power factor of microgrid.

In autonomous mode, the active power of VSC1 and VSC2 increased while the reactive power decreased due to the capacitor bank of 40kVAR at PCC.As a result, active power received from the grid is reduced, as seen in Fig.37. Fig.5.63 and Fig.5.64provide a clearer picture of the real and reactive power delivered to the loads.

Preprints (www.preprints.org) | NOT PEER-REVIEWED | Posted: 16 May 2022 doi:10.20944/preprints202205.0204.v1

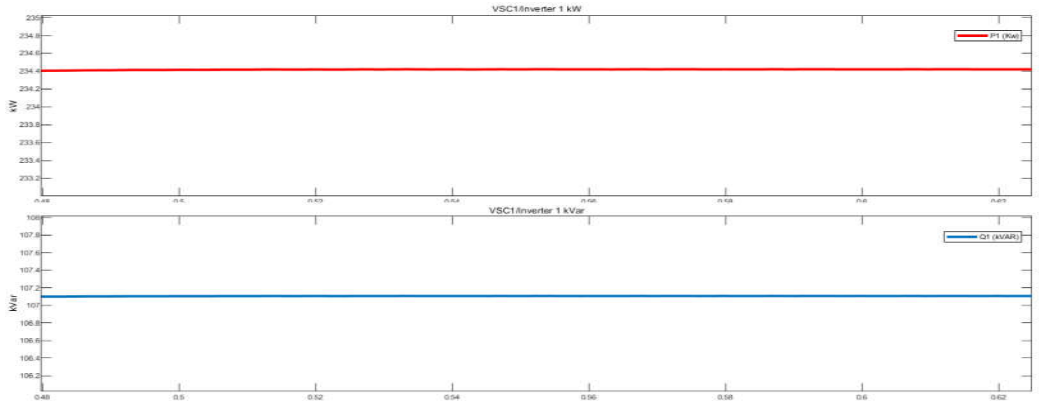

Figure 37. Enhanced VSC1 real and reactive power in island mode.

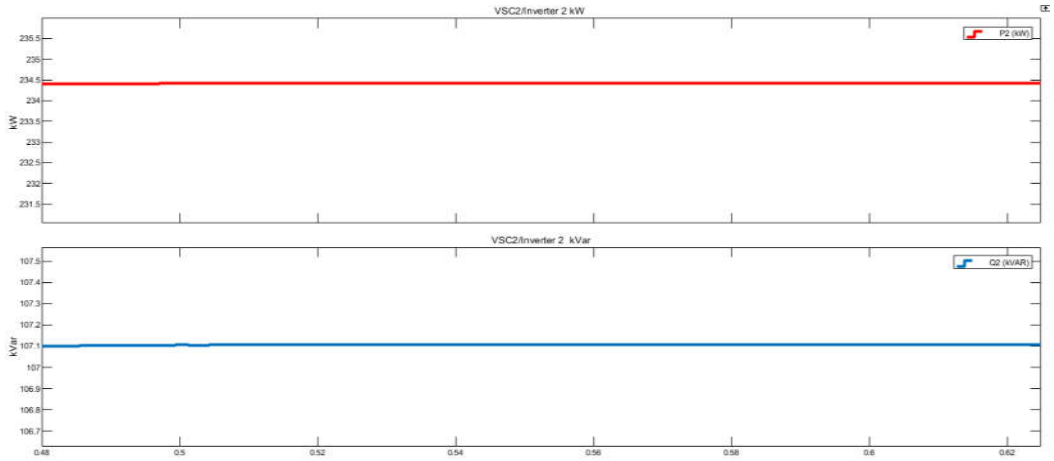

Figure 38. Enhanced VSC2 real and reactive power in island mode.

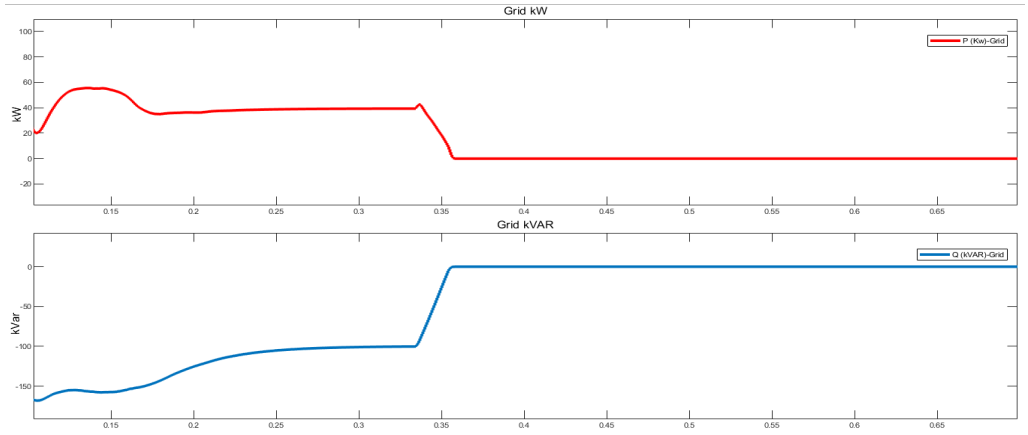

Figure 39. Enhanced grid active and reactive power.

Following the deployment of the capacitor bank, the voltage and current of the PCC are evaluated (see Fig.40). Fig.41 and Fig.42 show the corresponding voltage and current harmonic spectrums. The voltage THD decreased from 2.53 % to 0.76 %, while the current THD increased slightly from 2.56 % to 2.76 %, however, no single harmonic magnitude larger than 3% of the fundamental component was observed.

Preprints (www.preprints.org) | NOT PEER-REVIEWED | Posted: 16 May 2022 doi:10.20944/preprints202205.0204.v1

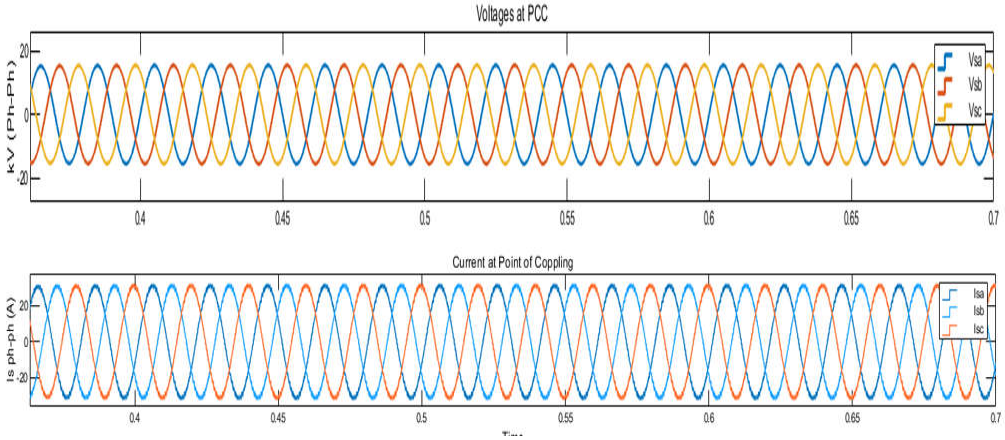

Figure 40. Enhanced Voltage and current waveform of PCC.

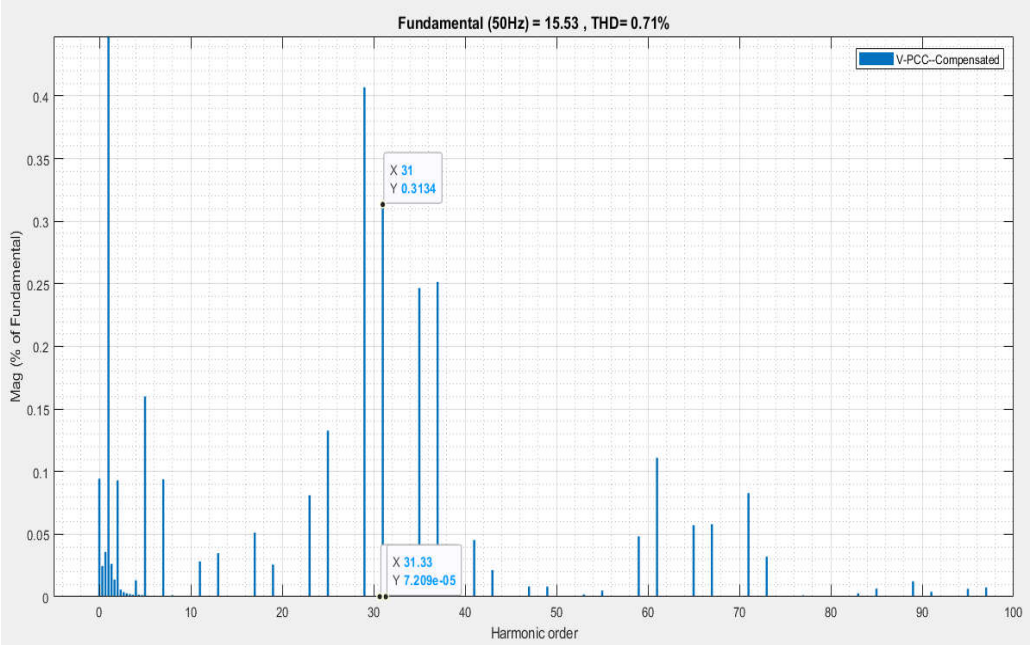

Figure 41. Voltage harmonic spectrum of PCC in autonomous mode.

Preprints (www.preprints.org) | NOT PEER-REVIEWED | Posted: 16 May 2022 doi:10.20944/preprints202205.0204.v1

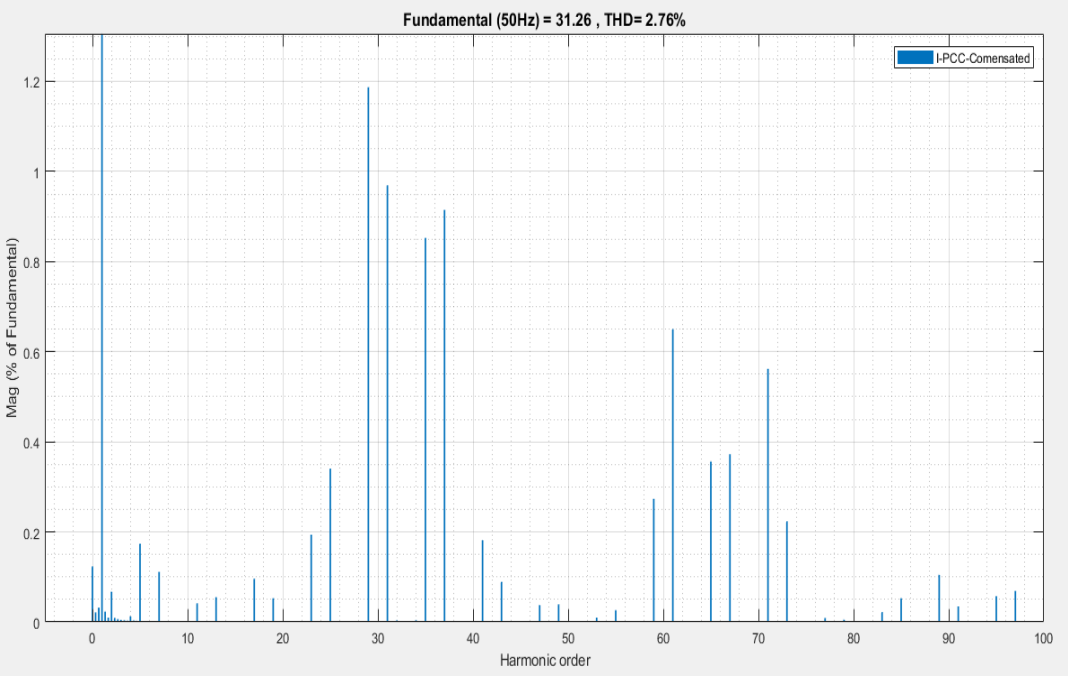

Figure 42. Current harmonic spectrum of PCC in autonomous mode.

When VSCs operating mode transitioned from grid to autonomous mode, a smooth and seamless transition was achieved, and the load was served with acceptable power quality. As a result, the research's objectives of using machine learning to operate parallel-connected VSCs, establishing a smooth and seamless transition from the grid to island mode, and enhancing power quality have been accomplished.

6. Conclusion:

The best performance of the proposed DNN-based MPPT controller and SRF-PLL is investigated and presented. Harmonic spectrums and total harmonic distortion in output voltage and current waveforms are evaluated, and no single harmonic more than 3% of the fundamental component is determined to be within the permitted range. The fixed capacitor bank $Qc \leq 15\%$ of transformer kVA i.e. 40kVAR is employed at PCC to enhance the power factor and the Simulink model is simulated again. It is determined that when the capacitor bank is employed at PCC, the power factor increased from 0.8667 to 0.9091 while THD of PCC voltage is reduced interestingly from 2.56% to 0.76%. The THD of PCC current is slightly increased from 2.55% to 2.76% which is again in the permissible range i.e. <5% with no single harmonic magnitude is greater than 3% of the fundamental component.

References

[1] Leila Sedghi, Masoud Emam, Ahmad Fakharian, and Mehdi Savagheb, "Decentralized control of an islanded microgrid based on offline model reference," *Journal of Renewable and Sustainable Energy*, p. 18, 2018.

[2] Asmus, Peter and Carol Stimmel, "Utility Distribution Microgrids. Research Report, Boulder," http://www.pikeresearch.com/blog/articles, 2012.

[3] L. Sedghi,A. Fakharian, "Robust Voltage Regulation In Island Mode: A LMI base Mixed H2/H infinity Control Approach," in *24th Mediterranean Conference on Control and Automation (MED)*, Athens, Greece, 2016.

[4] Seno D. Panjaitan,Rudi Kurnianto, Bomo W. Sanjaya, "Control of Parallel Inverters for High Power Quality and Sharing Accuracy in Single-phase AC Microgrids," in *2018 UKACC 12th International Conference on Control (CONTROL)*, Sheffield, UK, 2018.

[5] H. Mahmood, D. Michaelson, and J. Jiang, "Accurate Reactive Power Sharing in an Islanded Microgrid Using Adaptive Virtual Impedances," *IEEE Trans. on Power Electronics*, Vols. 30, no. 3, pp. 1605-1617, March 2015.

[6] Giri R., Choudhary V., Ayyanar R. et al., "Common-duty-ratio control of input-series connected modular DC–DC converters with active input voltage and load-current sharing," *IEEE Trans. Ind. Appl.,* Vols. 42, (4), p. 1101–1111, 2006.

[7] Kawabata T., Higashino S., "Parallel operation of voltage source inverters," *EEE Trans. Ind. Appl.,,* Vols. 24, (2), p. 281–287, 1988.

[8] De Brabandere K., Bolsens B., Van Den Keybus J. et al, "A voltage and frequency droop control method for parallel inverters," *IEEE Trans. Power Electron.,* Vols. 22, (4), p. 1107–1115, 2007.

[9] T. Caldognetto and P. Tenti, "Microgrids Operation Based on Master–Slave Cooperative Control," *EEE J. of Emerging and Selected Topics in Power Electronics,* Vols. 2, no. 4, pp. 1081 -1088, Dec. 2014.

[10] Y. Han, P. Shen, X. Zhao, and J. M. Guerrero, "An Enhanced Power Sharing Scheme for Voltage Unbalance and Harmonics Compensation in an Islanded AC Microgrid," *IEEE Trans. on Energy Conversion,* Vols. 31,no.3, pp. 1037-1050, Sept. 2016.

[11] Prodanovic M., Green T.C., Mansir H, "'A survey of control methods for three-phase inverters in parallel connection'.," *IEEE Conf. on power electronics and variable speed drives,* p. 472–477, Jordan, 2000.

[12] Siri K., Lee C., Wu T.-F., "Current distribution control for Para1le1 connected converters," *IEEE Trans. Aerosp. Electron. Syst.,,* Vols. 28, (3), p. 841–85, 1992.

[13] Sun X., Lee Y., Xu D, "Modeling, analysis, and implementation of parallel multi inverter systems with instantaneous average-current-sharing scheme," *IEEE Trans. Power Electron,* Vols. 18, (3), p. 844–856, 2003.

[14] Yanga J., Yuana W., Suna Y., "A novel quasi-master-slave control frame for PV-storage independent microgrid," *Electr. Power Energy Syst,* vol. 97, p. 262–274, 2018, .

[15] Guo F., Wen C., Mao J, "Distributed secondary voltage and frequency restoration control of droop-controlled inverter-based microgrids," *IEEE Trans. Ind. Electron.,* Vols. 62, (7), p. 4355–4364, 2015.

[16] Majumder R., Ghosh A., Ledwich G. et al.: ', "Angle droop versus frequency droop in a voltage source converter based autonomous microgrid," in *Proc. IEEE Power Energy Society General Meeting*, Calgary, AB, Canada, July 2009.

[17] A. Elmitwally and M. Rashed, , "'Flexible operation strategy for an isolated pv-diesel microgrid without energy storage," *IEEE Transactions on Energy Conversion,* vol. 26, p. 235–244, March 2011.

[18] Miftah Al Karim, Jonathan Currie, Tek-Tjing Lie, "A Distributed Machine Learning Approach for the Secondary Voltage Control of an Islanded Micro-Grid," in *2016 IEEE Innovative Smart Grid Technologies - Asia (ISGT-Asia)*, Melbourne, Australia, Nov 28 - Dec 1, 2016.

[19] S. S. Khorramabadi and A. Bakhshai, "Critic-based self-tuning PI structure for active and reactive power control of VSCs in microgrid systems," *IEEE Trans. Smart Grid* , vol. 6, p. 92–103, (2015).

[20] M. Taghizadeh, M. Mardaneh, and M. Sha Sadeghi, , "A new method of voltage and frequency control in isolated microgrids using enhanced droop controller optimized by frog algorithm," *J. Renewable Sustainable Energy* , vol. 6, pp. 013-136, (2014).

[21] M. S. Mahmoud and S. A. Hussain, "Adaptive PI secondary control for smart autonomous microgrid systems," *Int. J. Adapt. Control Signal Process,* vol. 29, p. 1442–1458, 2015.

[22] Z. Ullah, S. Wang, J. Radosavljevi ć, and J. Lai, "A solution to the optimal power flow problem considering WT and PV generation," *IEEE Access,* vol. 7, p. 46763–46772, 2019.

[23] T. Adefarati, R. C. Bansal, and J. J. Justo, , "Technoeconomic analysis of a PV–wind–battery–diesel standalone power system in a remote area," *Journal of Engineering,* vol. 13, p. 744, 2017.

[24] Adel Ab-BelKhair, Javad Rahebi,Abdulbaset Abdulhamed Mohamed Nureddin, "A Study of Deep Neural Network Controller-Based Power Quality Improvement of Hybrid PV/Wind Systems by Using Smart Inverter," *Hindawi International Journal of Photoenergy,* Vols. 2020, Article ID 8891469, p. 22, 2020.

[25] Jing Wang,Nicolás C. P. Chang, Xiaowei Feng, Antonello Monti, "Design of a Generalized Control Algorithm for Parallel Inverters for Smooth Microgrid Transition Operation," *IEEE TRANSACTIONS ON INDUSTRIAL ELECTRONICS,* no. DOI: 10.1109/TIE.2015.2404317, 2015.

[26] Amirreza Naderipour, Abdullah Asuhaimi Mohd Zin, "An improved synchronous reference frame current control strategy for a photovoltaic grid-connected inverter under unbalanced and nonlinear load conditions," *PLOS ONE | DOI:10.1371/journal.pone.0164856* , pp. 1-17, February 13, 2017.

[27] Remus Teodorescu, Marco Liserre and Pedro Rodríguez, GRID CONVERTERS FOR PHOTOVOLTAIC AND WIND POWER SYSTEMS, John Wiley & Sons, Ltd. ISBN: 978-0-470-05751-3, 2011.

[28] Nagaraju Pogaku,Milan Prodanovic',Timothy C. Green,, "Modeling, Analysis and Testing of Autonomous Operation of an Inverter-Based Microgrid," *IEEE TRANSACTIONS ON POWER ELECTRONICS,* Vols. 22, NO. 2, pp. 613-616, MARCH 2007.

[29] Waleed Al-Saedi ⇑ , Stefan W. Lachowicz, Daryoush Habibi, Octavian Bass, "Power quality enhancement in autonomous microgrid operation using Particle Swarm Optimization," *Electrical Power and Energy Systems* , vol. 42, p. 139–149, (2012).

[30] A. Q. Al-Shetwi, M. Hannan, K. P. Jern, A. A. Alkahtani, "Power quality assessment of grid-connected PV system in compliance with the recent integration requirements," *Electronics*, Vols. 9, no. 2 , pp. 366-388, 2020.

[31] Amirnaser Yazdani,Reza Iravani, Voltage-sourced converters in power systems : modeling, control, and applications, John Wiley & Sons, Inc, 2010.

[32] C. Bajracharya, M. Molinas, J. A. Suul, T. M. Undeland, "Understanding of tuning techniques of converter controllers for vsc-hvdc," in *Nordic Workshop on Power and Industrial Electronics (NORPIE/2008)*, Espoo, Finland, June 9-11,2008.

[33] "Park, Inverse Park and Clarke, Inverse Clarke Transformations MSS," Software Implementations User Guide,Microsemi (pp. 5-9).

[34] S.-K. Chung, "A phase tracking system for three phase utility interface," *IEEE Transactions on Power Electronics,*, Vols. 15, no. 3, p. 431–438, May 2000..

[35] L. Arruda, S. Silva, and B. Filho, "PLL structures for utility connected system," in *Proceedings of the IEEE Industry Applications Conference*, Chicago, IL, pp. 2655–2660, September 2001.

[36] F. Blaabjerg, R. Teodorescu, M. Liserre, A.V. Timbus, "Overview of control and grid synchronization for distributed power generation systems," *IEEE Trans. Ind. Electron.* , vol. 53 (5), p. 1398–1409, (2006).

[37] M.A. Aboushal,Mohamed M. Zakaria Moustafa, "A new unified control strategy for inverter-based micro-grid using hybrid droop scheme," *Alexandria Engineering Journal*, pp. 1-17, 2019.

[38] D. Abramovitch, "Phase-locked loops: a control centric tutorial," in *Proceedings of the American Control Conference*, Anchorage, AK, May 2002.

[39] I. F II, , "IEEE Recommended Practices and Requirements for Harmonic Control in Electrical Power Systems," IEEE, New York, USA , 1993.